AFRL-IF-RS-TR-2005-261
Final Technical Report
July 2005

INTEGRATED CHEMICAL FUEL MICROPROCESSOR FOR POWER GENERATION IN MEMS APPLICATIONS

Massachusetts Institute of Technology

APPROVED FOR PUBLIC RELEASE; DISTRIBUTION UNLIMITED.

The views and conclusions contained in this document are those of the authors and should not be interpreted as necessarily representing the official policies, either expressed or implied, of the Defense Advanced Research Projects Agency or the U.S. Government.

AIR FORCE RESEARCH LABORATORY
INFORMATION DIRECTORATE
ROME RESEARCH SITE
ROME, NEW YORK

STINFO FINAL REPORT

This report has been reviewed by the Air Force Research Laboratory, Information Directorate, Public Affairs Office (IFOIPA) and is releasable to the National Technical Information Service (NTIS). At NTIS it will be releasable to the general public, including foreign nations.

AFRL-IF-RS-TR-2005-261 has been reviewed and is approved for publication

APPROVED: /s/
WALTER A. KOZIARZ
Project Engineer

FOR THE DIRECTOR: /s/
JAMES A. COLLINS, Acting Chief
Advanced Computing Division
Information Directorate

REPORT DOCUMENTATION PAGE

Form Approved
OMB No. 074-0188

1. AGENCY USE ONLY (Leave blank)	2. REPORT DATE July 2005	3. REPORT TYPE AND DATES COVERED Final Sep 99 – Mar 04

4. TITLE AND SUBTITLE

INTEGRATED CHEMICAL FUEL MICROPRCESSOR FOR POWER GENERATION IN MEMS APPLICATIONS

5. FUNDING NUMBERS
G   - F30602-99-2-0544
PE - 63739E
PR - E117
TA - 00
WU - 51

6. AUTHOR(S)

Klavs F. Jensen

7. PERFORMING ORGANIZATION NAME(S) AND ADDRESS(ES)
Massachusetts Institute of Technology
Department of Chemical Engineering
MIT Room 66-566
77 Massachusetts Avenue
Cambridge MA 02139

8. PERFORMING ORGANIZATION REPORT NUMBER

N/A

9. SPONSORING / MONITORING AGENCY NAME(S) AND ADDRESS(ES)

Defense Advanced Research Projects Agency   AFRL/IFTC
3701 North Fairfax Drive   26 Electronic Parkway
Arlington VA 22203-1714   Rome NY 13441-4514

10. SPONSORING / MONITORING AGENCY REPORT NUMBER

AFRL-IF-RS-TR-2005-261

11. SUPPLEMENTARY NOTES

AFRL Project Engineer: Walter A. Koziarz/IFTC/(315) 330-2536   Walter.Koziarz@rl.af.mil

12a. DISTRIBUTION / AVAILABILITY STATEMENT

APPROVED FOR PUBLIC RELEASE; DISTRIBUTION UNLIMITED.

12b. DISTRIBUTION CODE

13. ABSTRACT *(Maximum 200 Words)*
This document reports results obtained via "Integrated Chemical Fuel Microprocessor for Power Generation in MEMS Applications" during the performance period, 1 September 1999 – 31 March 2004. The overall goal of this program was to demonstrate a chemical fuel processing microsystem for power generation in MEMS applications. The program had several major accomplishments: 1. Development and fabrication of a new, thermally efficient, suspended tube MEMS heat exchanger/fuel processor. 2. Design and fabrication of a thermoelectric (TE) MEMS device for direct conversion of catalytic combustion energy into electrical power. 3. Demonstration of integration of the suspended tube MEMS heat exchanger/fuel processor and GaSb solar cell into the first MEMS based thermophotovoltaic (TPV) system with net energy output. 4. Development of MEMS devices for hydrogen purification, such as removing unreacted fuels. 5. Evaluation of system performance for different fuels and configurations. 6. Exploration of microfabricated entrainment based pumps as potential options for air injection in microburner systems.

14. SUBJECT TERMS
Micro-Electro-Mechanical Systems (MEMS), Fuel, Cell, Processor, Heat Exchanger, Microfabricated Pump

15. NUMBER OF PAGES 40

16. PRICE CODE

17. SECURITY CLASSIFICATION OF REPORT	18. SECURITY CLASSIFICATION OF THIS PAGE	19. SECURITY CLASSIFICATION OF ABSTRACT	20. LIMITATION OF ABSTRACT
UNCLASSIFIED	UNCLASSIFIED	UNCLASSIFIED	UL

Table of Contents

List of Figures

List of Tables

EXECUTIVE SUMMARY

This final report describes accomplishments made in the DARPA micropower program (MPG), "Integrated Chemical Fuel Microprocessor for Power Generation in MEMS Applications," (F30602-99-2-0544) during the performance period. The overall goal of this program was to demonstrate a chemical fuel processing microsystem for power generation in MicroElectroMechanical Systems (MEMS) applications. The program had several major accomplishments:

1. Development and fabrication of a new, thermally efficient, suspended tube MEMS heat exchanger/fuel processor. Experiments with this device led to the first demonstration of net hydrogen production in a MEMS based fuel processor. Combustion and hydrogen production was demonstrated with hydrocarbons and ammonia.

2. Design and fabrication of a thermoelectric (TE) MEMS device for direct conversion of catalytic combustion energy into electrical power. This device used a thin catalytic membrane with integrated SiGe based TE elements and was able to operate autothermally, i.e., with no external energy input. The work represented the first demonstration of net electrical energy production in hydrocarbon powered MEMS TE generators.

3. Demonstration of integration of the suspended tube MEMS heat exchanger/fuel processor and GaSb solar cell into the first MEMS based thermophotovoltaic (TPV) system with net energy output.

4. Development of MEMS devices for hydrogen purification, such as removing unreacted fuels (ammonia and hydrocarbon) and carbon monoxide that could otherwise adversely affect hydrogen Proton Exchange Membrane (PEM) fuel cell performance.

5. Evaluation of system performance for different fuels and configurations, including different fuel cell options.

6. Exploration of microfabricated entrainment based pumps as potential options for air injection in microburner systems.

Details on these technical accomplishments are summarized in this final report. Additional information is provided in the publications resulting from this study. Members of the original project team have licensed the MEMS suspended-tube reactor/heat exchanger developed in this program to start a new company, Lilliputian Systems Inc. This company has successfully transferred the fabrication and testing of a MIT suspended-tube reactor/heat exchanger. The company aims to combine the hydrogen reforming concepts of the Defense Advanced Research Program (DARPA) program with microfabricated solid oxide fuel cells (SOFCs) into an integrated, portable fuel-to-electrical power generator. The company has received Advanced Technology Program (ATP) funding and has successfully completed several rounds of financing. Based on the device work done in the MEMS DARPA program, the Principal investigator and a team of MIT faculty proposed and were granted a Multidisciplinary University Research Initiative (MURI) from the Army Research Office to develop the knowledgebase for microchemical

systems for conversions of fuels to electrical energy. This MURI program continues to investigate thermally efficient MEMS based systems for fuel processing and Pd purification systems along with micro SOFCs.

1. MEMS HEAT EXCHANGER REACTOR FOR HYDROGEN GENERATION

We have designed and fabricated a MEMS suspended-tube reactor/heat exchanger to thermally isolate the chemical reaction zone in a power generation system. It overcomes the thermal management difficulties of small-scale fuel processors through the integration of thermally-insulating and thermally-conductive materials in a carefully defined, microfabricated tube/slab structure.

The suspended-tube reactor (Figure 1) is designed to simultaneously carry out two reactions that exchange heat: a combustion reaction to generate the heat, and an endothermic reaction to produce hydrogen. A variation of this reactor is also designed for thermophotovoltaic power generation (discussed in subsequent section). The main components are four thin-walled (2-µm wall thickness), U-shaped, 3-mm long tubes made of low-stress silicon nitride.
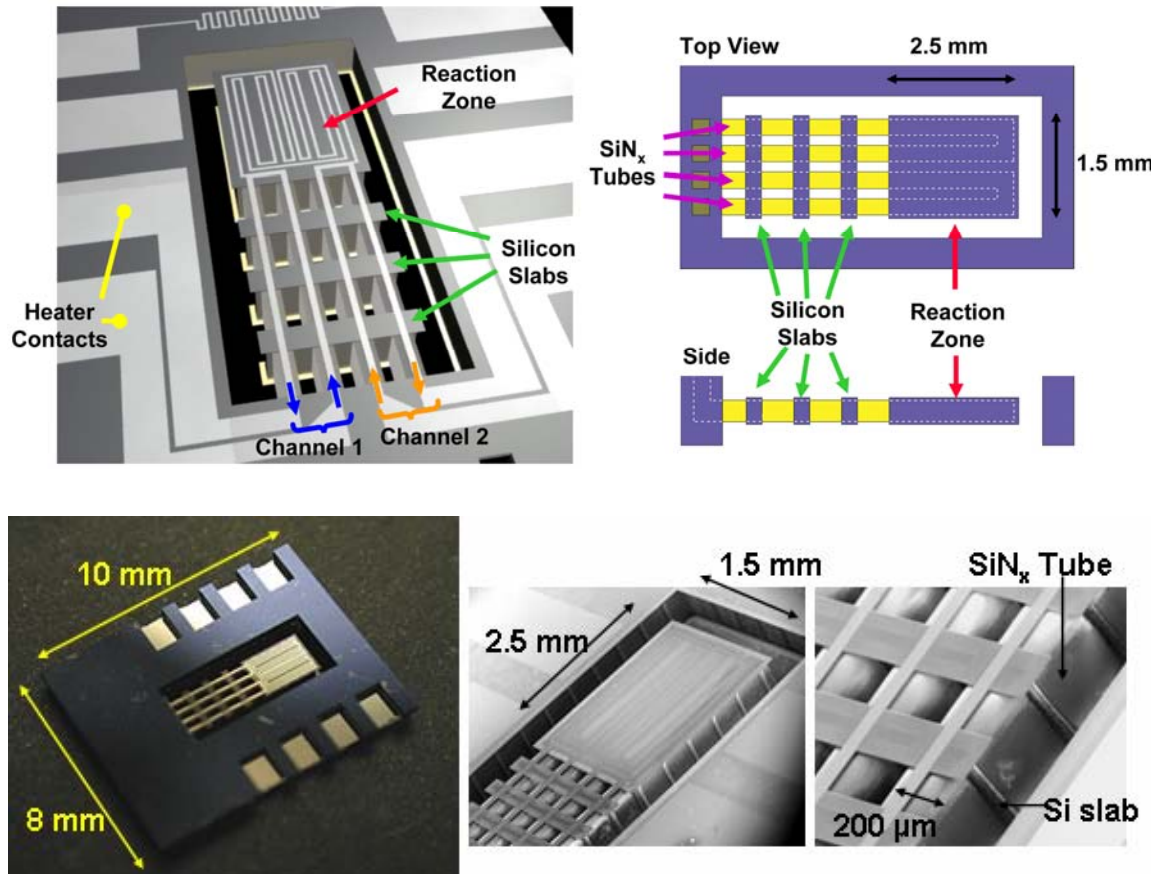
Figure 1. The suspended-tube reactor. In the fabricated device, each tube is 200 µm wide by ~480 µm high. While a three-slab configuration is shown in this figure, the number of slabs can be varied. The silicon slabs wrap completely around each.

2

The reactions take place in adjacent channels at the suspended end of the silicon nitride tubes, within a thermally-conductive silicon reaction zone. Heat exchange in this zone is facilitated by the intimate thermal contact between the channels, and by the silicon that encases the tubes in this region. The suspended silicon nitride tubes contain slabs of silicon positioned along the length of the tubes to exchange heat between process streams and recover process energy from the exhaust gases.
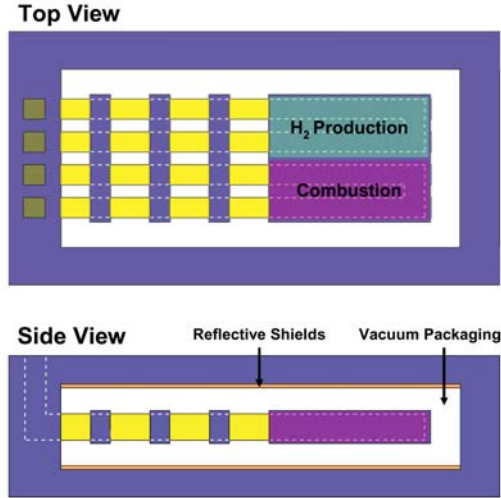
Figure 2. Illustration of how the suspended-tube reactor is used for simultaneous combustion and hydrogen production. The combustion heats up the entire silicon reaction zone at the end of the tubes so that endothermic hydrogen production may take place. Vacuum packaging and reflective shields, required to maximize the thermal isolation of the reaction zone, have been tested independently, but have yet to be integrated into the device.

This design of the suspended-tube reactor was intended to be flexible for various fuel processing options. For hydrogen production through endothermic reactions (e.g., ammonia cracking, hydrocarbon steam reforming), combustion of a fuel in one stream provides the energy required for the endothermic reaction in the adjacent stream (as shown in Figure 2), and both streams are kept in intimate thermal contact. For exothermic hydrogen production (e.g., partial oxidation of hydrocarbons), both channels can be used to process the reactant mixture, and the structure serves as a thermally-isolated reactor/preheater. The suspended-tube reactor can also be used as a thermally-efficient combustor/recuperator in other power generation systems, such as in TE or TPV generators. Tests of the suspended-tube reactor for TPV generation are discussed in a subsequent section.

1.1 <u>Overall Heat Loss and Energy Balance</u>

The experimental steady-state heat loss analyses (in the absence of flow) and the numerical heat recuperation analysis provide a thorough description of the overall heat losses in the suspended-tube reactor. This detailed understanding of the heat losses is required in order to make meaningful predictions of reactor performance, whether the reactor is used for hydrogen

production or as a combustor (for TE or TPV). The heat losses affect the overall efficiency and influence the steady-state reactor temperature for autothermal (self-sustained) combustion.

The steady-state heat loss analysis and heat recuperation analysis combine to describe the overall heat loss in the suspended-tube reactor. For zero flow rates within the tubes, heat will be lost by conduction along the tubes, conduction and natural convection in the air, and through radiation. For nonzero flow rates within the tubes, energy will also be lost via forced convection. The overall heat loss from the reactor can be approximated as the sum of all these contributions to the heat loss.

Figure 3 shows the predicted overall steady-state heat loss based on combined data from steady-state heat loss experiments and numerical modeling of the heat recuperation at 800ºC. The y-intercepts for the three curves represent the experimentally measured steady-state heat losses in the absence of flow. The highest value of the intercept corresponds to the overall heat loss measured at atmospheric pressure, the next value corresponds to the overall heat loss measured under vacuum, and the lowest value (with perfect shields) represents the upper estimate for the heat loss due solely to conduction in the solid.

Figure 3. **Predicted steady-state heat loss in the suspended-tube reactor as a function of flow rate within the four tubes**

The overall heat loss can be used in an energy balance analysis in order to make predictions of reactor performance. With combustion occurring in the silicon reaction zone, the energy generated by the combustion reaction at steady-state will equal the heat loss from the reactor. If an endothermic reaction is occurring in the second channel in the reaction zone, then some of the combustion energy will also be "consumed" by this reaction (as the products are transferred to a higher thermodynamic energy state than the reactants). Two situations will be considered: (1) combustion in one channel (where another reaction would be taking place in an adjacent channel to produce hydrogen) and (2) combustion in both channels (e.g. for TE and TPV generation, see Section 4).

For the heat balance analysis, it was assumed that the fuel combusts to completion, i.e. (conversion is 100%), and that this combustion is the only source for heat generation in the reactor. The ratio of heat generated to heat lost is maximized when all of the fuel fed to the reactor is converted. Therefore, the results obtained from the heat balance where full conversion was assumed to represent the best possible scenario for thermal management in the reactor. In reality, the fuel conversion may be below 100% for the combustion reactions due to finite reaction rates within the relatively small reactor volume (and small catalyst mass). Accurate predictions for the reaction rates require detailed modeling of the kinetics, heat, and mass transfer within the reactor.

4

For hydrogen production, combustion in one channel drives an endothermic reaction in the other channel. In this case, all of the energy released by combustion of the fuel is either lost to the environment or consumed by the endothermic reaction. Figure 4 shows the predicted heat loss and heat generation as a function of flow rate for a reactor at 400ºC and 800ºC.
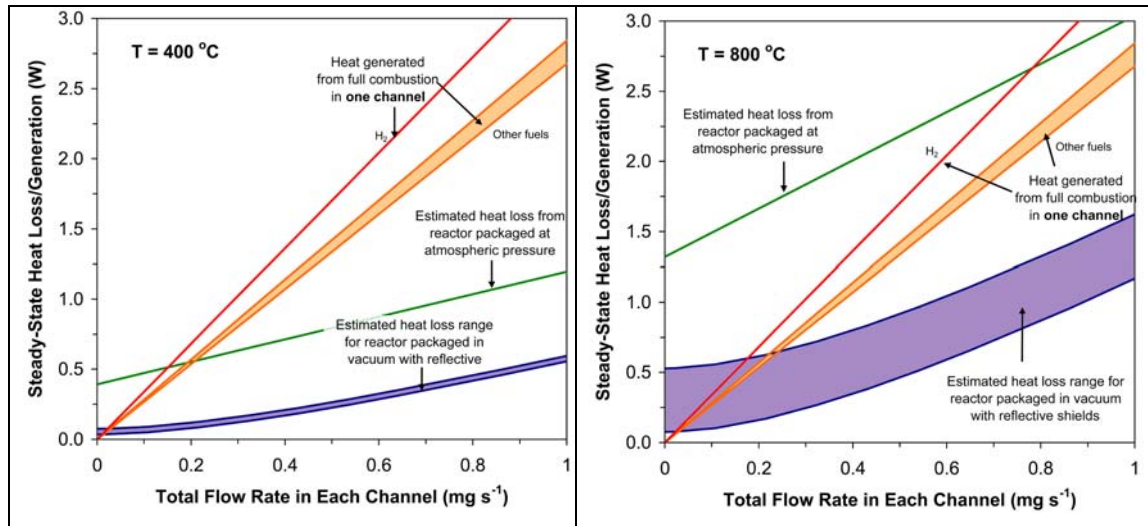
Figure 4 Predicted steady-state heat loss and heat generation for a reactor at 400ºC and 800ºC as a function of flow rate within each tube. The generation lines correspond to full conversion of a stoichiometric fuel/air mixture at the given flow rate in one channel. The "other fuels" includes butane, propane, methanol, and ammonia. The heat loss assumes that the flow rate in both channels is equivalent.

The heat losses from a reactor at 800ºC were much more significant, so the corresponding fuel requirements in this case are much higher. In fact, for the range of flow rates considered in this analysis, the fuels other than hydrogen cannot be burned autothermally for a reactor packaged in air. This means that reaction zone must be able to completely combust more than 10^{-6} kg of a stoichiometric fuel/air mixture per second (thereby generating well over 2.5 W of thermal power) in order to reach a steady state. Hydrogen, however, can be burned autothermally in a reactor packaged at atmospheric pressure with substantially lower flow rates and heat loss. A reactor packaged in vacuum has substantially lower fuel requirements. This is due to both the substantially reduced heat loss in the absence of flow and the heat recuperation that can be achieved by a reactor packaged in vacuum. For a reactor at 800ºC, the influence of the reflective shields on the fuel requirements is substantial.

The suspended-tube reactor may also potentially be used as a combustor for other forms of portable electric power generation (including TE and TPV, Section 4). In this case, both channels of the suspended-tube reactor would be used for combustion. Figure 5 shows the predicted heat loss and heat generation for a reactor at 800ºC in which combustion proceeded at full conversion in both channels. In this case, the heat balance closes for all of the fuels within the range of flow rates considered. The total flow rate of fuel and air in both channels when combustion occurs in both channels is substantially lower than that required for a reactor at 800ºC in which combustion occurs only in one channel. Using hydrogen, for example, a total fuel/air flow rate (in both tubes) of ~0.5×10^{-6} kg·s^{-1} is required to maintain the reactor at 800ºC when combustion occurs in both

channels, whereas a total fuel/air flow rate of ~0.8×10^{-6} kg·s^{-1} is required when combustion occurs in only one channel. Correspondingly, the heat loss in a reactor at 800ºC (at atmospheric pressure) with combustion in both channels is ~1.7 W, whereas with combustion in only one of the channels is ~2.6 W. This difference corresponds to the additional heat carried off by the extra stream in the case where combustion occurs in only one channel.
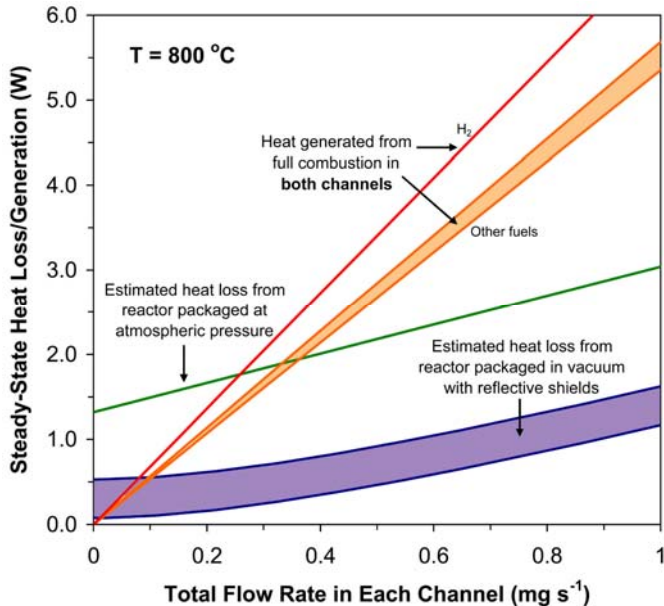
Figure 5. Predicted steady-state heat loss and heat generation for a reactor at 800ºC as a function of flow rate within each tube.

1.2 Catalyst Preparation and Localization Using Fluidic Stop Valves

Fuel processing for hydrogen production requires elevated temperatures. Some of the processes, including combustion, can in theory be carried out homogeneously, i.e. without a catalyst. However, for all types of reactions, a catalyst can reduce the temperature requirements for the reactions significantly, and thereby reduce the heat losses from the system. For this reason, fuel processing systems, particularly those used for portable power generation, extensively employ heterogeneous catalysts.

Various types of catalysts can be used within microchannels, including particles or pellets, catalysts directly impregnated into the microchannel walls, or washcoats of supported catalysts. Regardless of what type of catalyst is used, localization of the catalyst is an important component of the catalyst preparation. The suspended-tube reactor can not be disassembled in order to load the catalyst directly in a particular region of the reactor. In the suspended-tube reactor, passive fluidic stop valves have been integrated for localization of catalysts prepared by washcoating techniques.

Figure 6 outlines the general procedure for using a stop valve to control the location of the catalyst, and thereby control the location of the catalytic combustion. Prior to loading of the catalyst, the surfaces may need to be treated to modify the wetting properties of the washcoat solution on the surface. The liquid catalyst solution was first allowed to wick in via the outlet tube of the combustion channel. So long as the liquid wet the solid (contact angle below 90º) and

no sudden enlargements were present along the way to the stop valve, the liquid wicks into the channel and reaction zone without the need for applied pressure. When the liquid reached the sudden enlargement at the stop valve, the liquid no longer continued to flow into the channel. If the stop valve is placed at the reaction zone inlet, it may prevent the washcoat solution from entering the inlet tube. Once the catalyst dried, catalyst was only present within the reaction zone and outlet tube, but not in the inlet tube. The catalyst at this point can be calcined and/or reduced *in situ*. To carry out the reactions, the combustion gases (fuel/air mixture) are then introduced through tube that does not contain catalyst and therefore will not ignite prior to reaching the reaction zone.
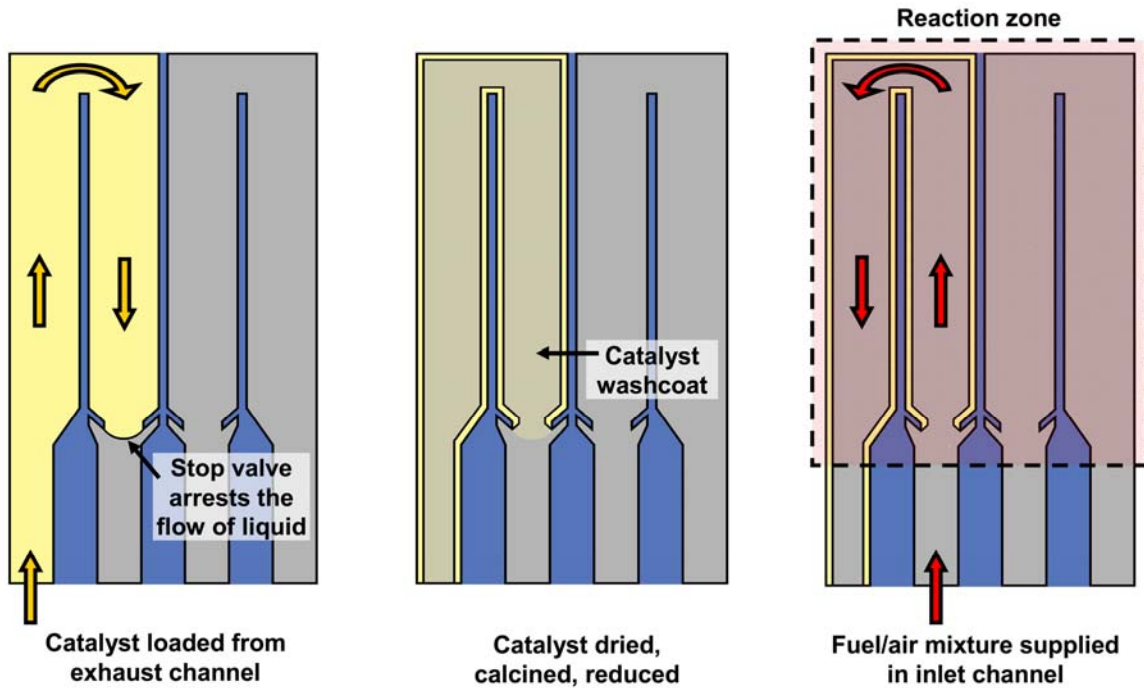
Figure 6. Procedure for introducing catalyst washcoats such that catalyst was not deposited in the inlet tube.

Through an energy minimization analysis, it is possible to estimate the stop pressure (pressure opposing the continued flow of the liquid) that develops at the fluidic stop valve. For a positive stop pressure, the fluid will reach the stop valve and cease to flow. The sign and magnitude of the stop pressure are determined by several factors, including the valve angle (β), the contact angle (θ), the width of the channel (h) and the liquid vapor surface tension (γ_{LV}).

Various silanes were tested for modifying the surface of the silicon nitride. n-octyltriethoxysilane (OTS, United Chemical Technologies) was effective at increasing the hydrophobicity of the surface just enough to allow the stop valve to work without preventing the catalyst solution from wicking into the tubes. Stop valves with silicon, silicon dioxide, and silicon nitride surfaces modified with OTS can effectively arrest the fluid flow. Figure 7 shows aqueous liquid loaded effectively into the fluidic channels of the reactor and held at the stop valve.
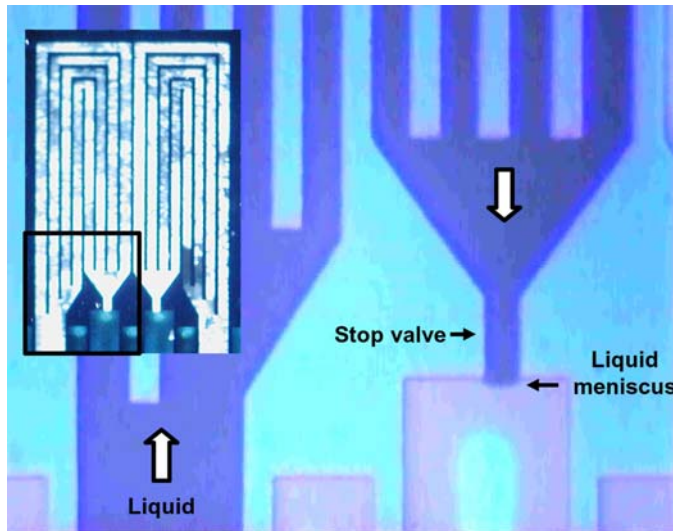
Figure 7. Enhanced contrast micrograph of water loaded into a channel containing a fluidic stop valve. The surfaces have been silanized with OTS to increase their hydrophobicity. The inset shows how this technique can be used to control the catalyst deposition within the suspended-tube reactor (catalyst is white). A glass-capped, oxidized silicon test wafer was used for the visualization.

1.3 <u>Chemical Reaction Testing</u>

The suspended-tube MEMS fuel processor was designed to generate hydrogen in a high-temperature reaction zone. Within this zone, two distinct reactions take place. In one channel, a fuel is combusted over a catalyst to generate heat. This heat allows the entire reaction zone to be maintained at an elevated temperature with no electrical power input at steady-state. In addition, this heat is used by an endothermic process occurring in the second channel, in which a fuel (not necessarily the same fuel used for the combustion) reacts over a catalyst to form hydrogen and other side products. Various fuels, such as hydrogen, ammonia, methanol, propane, or butane (or combinations of these) can be used on the combustion side. Similarly, several fuels can be used on the endothermic side. For example, hydrocarbon or alcohols can be processed via steam reforming to produce hydrogen. Alternatively, ammonia or methanol can be decomposed (cracked) catalytically to generate hydrogen.

For the evaluation of the fuel processor, two reaction systems were considered: (1) catalytic combustion (various fuels), and (2) catalytic ammonia cracking. Product gas compositions are analyzed online with a time-of-flight mass spectrometer (Inficon H300M Transpector) and a micro gas chromatograph with thermal conductivity detection (Agilent, PPU 6 and MolSieve 5A columns). Simulated air with 79 mol % Ar and 21 mol % O_2 was used for combustion reactions to circumvent mass spectrometry deconvolution of ion 28.

All of the present results were performed in 7-slab reactors with the parallel microchannel reactor design with functional stop valves and calibrated Ta/Pt/Ta heaters. These reactors had several practical advantages over the other designs, including facilitated loading of catalyst, lower pressure drop, larger combustor volume, and the 7-slab structure which generally was more robust than the 3-slab structures during routine handling and for vacuum testing.

Simultaneous butane combustion and ammonia cracking were carried out in the suspended-tube reactor over washcoated catalyst particles. The catalysts used in this study were deposited from aqueous slurries containing fine powders of 1 wt.% Pt on La-doped γ-Al$_2$O$_3$ (Alcoa Ga-200LSF Alumina) reduced *ex-situ* in 100% H$_2$ at 300ºC. Figure 8 shows a photograph taken during autothermal butane combustion and ammonia cracking in the suspended tube reactor. As the photograph (Figure 8) shows, combustion occurred within the silicon reaction zone, as well as within a small section of the exhaust tubing. The ammonia cracking channel within the reaction zone did not appear to be as bright as the combustion channel. During theautothermal portion of this experiment, net hydrogen was achieved from the reactor with no electrical power input.
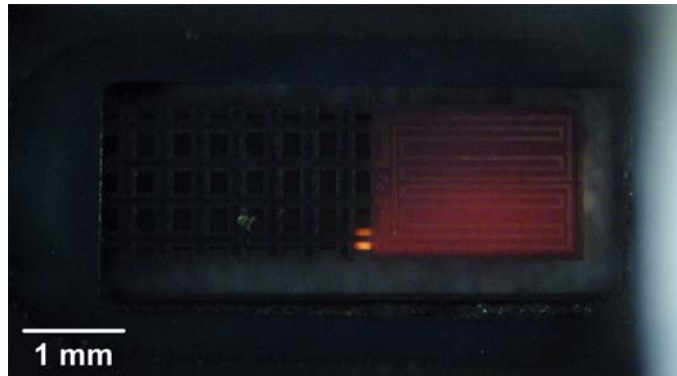
Figure 8. Photograph of simultaneous butane combustion and ammonia cracking in the suspended-tube reactor. Autothermal combustion of a butane/air mixture is taking place in the bottom channel while ammonia cracking is taking place in the top channel.

Hydrogen combustion occurred to full conversion (> 99%) throughout a broad range of flow rates (Figure 9). The hydrogen ignited after slight heating with the integrated heaters (and in some cases from the heating within the testing fixture, which was maintained at ~120ºC during combustion experiments). Through hydrogen combustion combined with ammonia cracking, significant production rates of H$_2$ were demonstrated from ammonia. However, the catalytic hydrogen combustion reaction could run away if the reactor temperature became too high, resulting in reactor failure. This situation can be avoided through proper control of the fuel feed rates. Hydrogen combustion and ammonia conversion were carried out autothermally in a controlled fashion. In this case, stable steady states were achieved by limiting the flow rates of the combustion gases to the reactor.

Figure 10 shows the autothermal combustion temperatures achieved stably in the suspended-tube reactor during autothermal combustion. Plotted along side is the predicted autothermal combustion temperature based on full conversion of the hydrogen feed with no heat recuperation (based on the energy balance analysis presented in above). The predicted autothermal combustion temperature, which was based on a simple energy balance analysis, is 50-100ºC lower in temperature than the measured values throughout the entire range of flow rates. This difference is attributed to assumptions of the model, in particular the model not accounting for heat recuperation in the tube/slab structure.
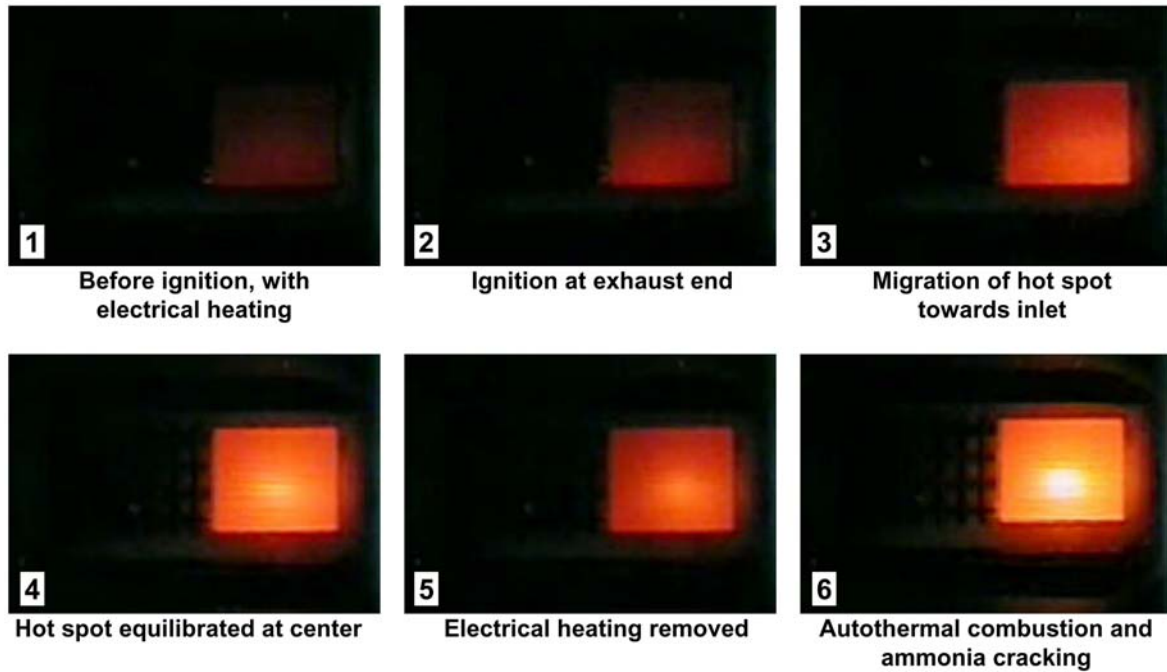
Figure 9. Sequence of images (over the course of ~ 10 s) showing the ignition of a hydrogen in the bottom channel of the reactor, with ammonia flowing in the top channel.
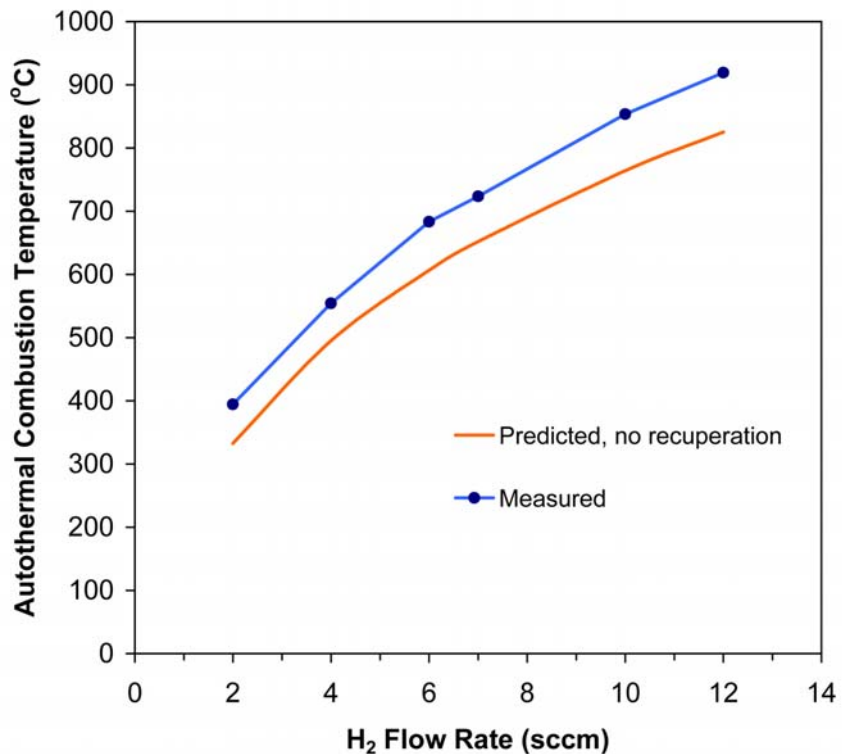
Figure 10. Measured and predicted (for full conversion with no heat recuperation) autothermal combustion temperatures in the suspended-tube reactor during autothermal hydrogen combustion (in simulated air) and ammonia cracking. For all of these points, the measured hydrogen conversion on the combustion side is >99.6%.

Ammonia combustion and ammonia cracking have been carried out under vacuum (using the vacuum testing fixture described in 5.3.2) over Pt on La-doped γ-Al$_2$O$_3$ catalysts. In the first series of experiments, autothermal ammonia cracking was carried out independently at a pressure of ~30 mTorr as the flow rate of ammonia was varied. In the second set of experiments, autothermal ammonia combustion with simultaneous ammonia cracking was carried out at a fixed flow rate of reactants as the ambient pressure was varied. Stable autothermal ammonia combustion with simultaneous ammonia cracking was observed between ambient pressures of 200 and 850 mTorr (Figure 11).
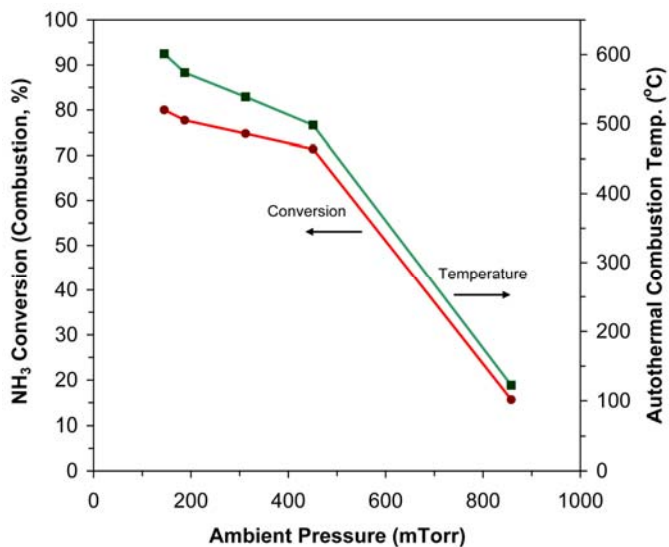
Figure 11. Ammonia conversion (stoichiometric combustion in simulated air) and autothermal reaction temperature as a function of ambient pressure during simultaneous combustion/cracking. Ammonia flow rate to the combustion side is 2 sccm. Ammonia flow to the cracking side is 10 sccm.

Ammonia cracking has been demonstrated in several different experiments. In addition, homogeneous fuel combustion has been demonstrated using various fuels. Table 1 summarizes the results from the ammonia cracking. Table 2 summarizes the autothermal combustion results. Refinements in the suspended tub burner concept are also discussed in connection with TPV devices in Section 4.

1.4 <u>Vacuum Packaging</u>

In order to minimize heat loss to the ambient, the reactor/heat exchanger must be packaged in vacuum. This is true whether it is generating hydrogen (fuel processing) or electricity through TE or TPV. We determined experimentally (consisted with model predictions) that above ~ 1 Torr, pressure had a limited effect on heat loss from the reactor. Between ~ 1 Torr and ~ 40 mTorr, heat loss decreased with pressure. Below ~ 40 mTorr, ambient pressure again had little effect on heat loss. These results set the target pressure for the vacuum package to be 40 mTorr or less.

We made significant progress towards achieving a reliable vacuum package for the suspended tube reactor. First we designed and fabricated a vacuum sensor test structure to use in place of the reactor/heat exchanger for evaluating vacuum bonding techniques. Second, we assembled a vacuum bonding system that allows us to bring chips into contact at temperature up to 600°C

while under vacuum. Finally, we evaluated the bonding characteristics of a commercially available glass frit.

Table 1. Ammonia Cracking Summary

Run	Heating Method	Catalyst	NH$_3$ Feed (sccm)	Temp. (ºC)	Peak Conv. (%)	Peak H$_2$ Prod. (μmol·s^{-1})	Peak H$_2$ Prod. (W$_{LHV}$)
1	Heater, 2.4W	Ir	16	>800 (est.)	26	1.1	0.27
2	Heater, 1.8W	Ir/Al$_2$O$_3$	6	>800 (est.)	97	6.5	1.6
3	Butane comb.	Pt/La-Al$_2$O$_3$	12.5	680	3	0.4	0.10
4	H$_2$ comb.	Pt/La-Al$_2$O$_3$	12.5	> 936	89	8.2	2.0
5	H$_2$ comb.	Pt/La-Al$_2$O$_3$	12	930	1	0.1	0.03
6	NH$_3$ comb.	Pt/La-Al$_2$O$_3$	10	600	0.06	0.006	0.002

Table 2. Summary of Autothermal Combustion of Fuel/Air

Fuel	Catalyst	Fuel Flow (sccm)	Conv. (%)	Heat (W)	Temp. (ºC)	Comments
Butane	Pt/Al$_2$O$_3$	0.44	90	0.80	-	Unstable
Butane	Pt/La-Al$_2$O$_3$	0.63	65	0.83	700	Unstable
Propane	Pt/La-Al$_2$O$_3$	2.0	46	1.4	770	Stable with combustion in both channels (for TPV)
H$_2$	Pt/La-Al$_2$O$_3$	2-12	>99	2.2	400-930	Stable up to 12 sccm fuel flow
NH$_3$	Pt/La-Al$_2$O$_3$	2-6	92-68	0.3-1.0	590-650	Under vacuum

The thermal conductivity vacuum sensor test structure (Figure 12) had a surface topography in the bonding area similar to the suspended-tube reactor (i.e. Ti/Pt lines between 100 and 200 nm high on silicon nitride, but included a more sensitive vacuum sensor and was much easier to fabricate. The assumption was that if a vacuum packaging technique could be successfully built around this test structure, the same techniques could be transferred directly to the suspended-tube reactor.

(a)

(b)
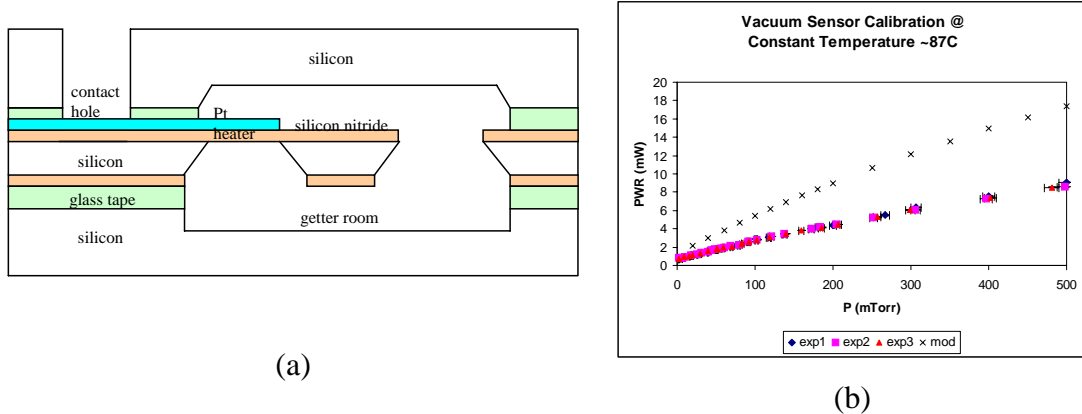
Figure 12. (a) Vacuum packaging schematic and (b) sensor calibration data (3 separate devices plotted with model prediction)

The die-level vacuum bonding apparatus is shown in Figure 13. A glass bell jar sits on top of a stainless steel feedthrough collar with a rubber gasket in between, which in turn sits on top of a stainless steel base plate with a rubber o-ring. A special stainless steel bonding chuck, placed inside the vacuum chamber for bonding, was made to align the three-layer stack of the test structure. This two-piece chuck has pre-drilled holes for cartridge heaters and thermocouple. The sample being bonded is placed inside the cavity of the bottom piece and sandwiched by the top piece. Cartridge heaters were used to heat up the glass frit to its softening point to initiate bonding. One or two stainless steel blocks placed on top of the chuck were used to provide pressure to the bonding interface.

Development of the vacuum bonding technique proved to be a greater challenge than initially envisioned in this project. We have continued to develop vacuum bonding approaches for the fuel processor under another project and we have identified bonding procedures that should enable bonding of the fuel processor devices.
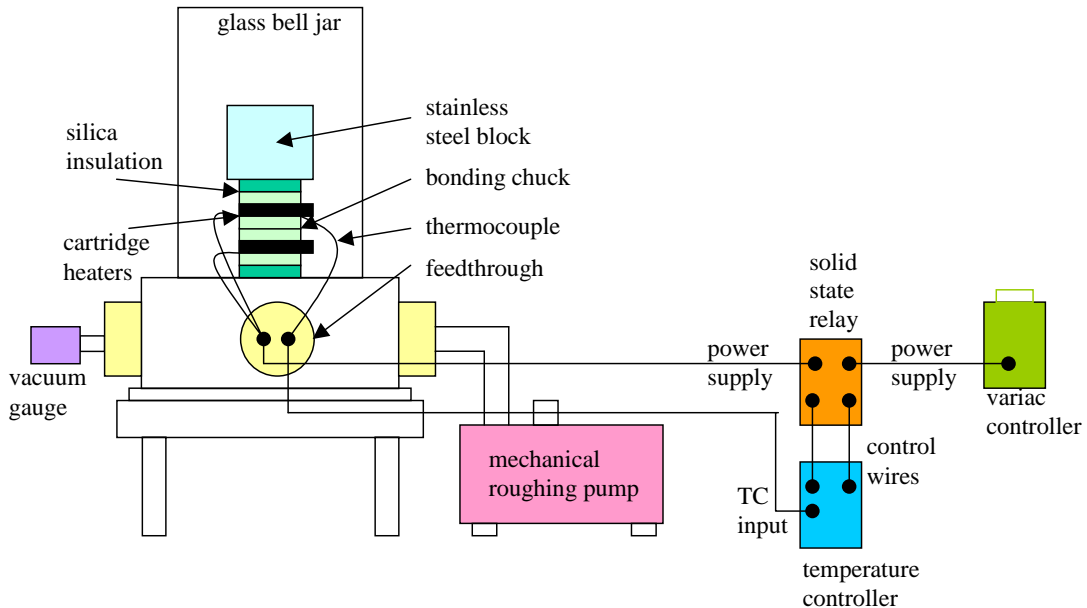
Figure 13. Die-level bonding apparatus

2. MEMS THERMOELECTRIC POWER GENERATION

A MEMS thermoelectric power generator with integrated catalytic combustion was microfabricated and successfully demonstrated. Electrical power output has been generated from on-chip autothermal combustion of a hydrogen-air mixture, with external power used only to drive mass-flow controllers. The device was operated at temperatures up to 750ºC, with thermopile voltages up to 6V. The theoretical efficiency of our silicon germanium (SiGe) thermoelements is above 5% at these temperatures. The demonstration device efficiency was well below 0.1% due to compromises in the first realization; however, this efficiency was in line with theoretical predictions and could be improved in subsequent designs with a potential of achieving above 5% efficiency. Our thermoelectric generator constituted the *first* reported demonstration of an integrated, continuous operation, chemical to electrical energy converter on a MEMS relevant scale.

The thermoelectric generator, (Figure 14) consisted of a channel etched in silicon and capped by a thin silicon nitride membrane. Sections of the channel side of the membrane are selectively coated with a combustion catalyst, usually platinum, using a self-aligned shadowmask. On the topside of the membrane, thermopiles have been patterned with the hot junctions down the center of the membrane and the cold junctions on the silicon at the channel's edge. The

Figure 14. Schematic of the thin-wall MEMS TE generator

thermoelectric materials used in the thermopiles were highly doped n- and p-type poly-SiGe. SiGe was chosen for its excellent high temperature conversion efficiency and ease of integration. A resistive heater was included for use during start-up and testing.
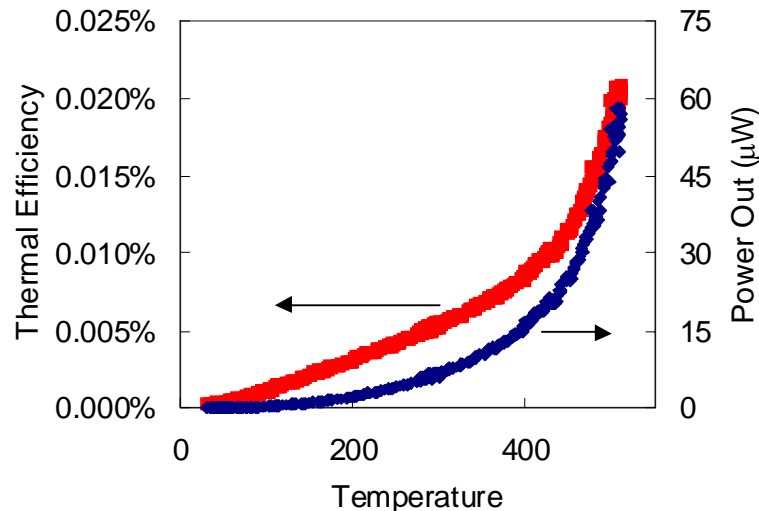
Figure 15. Thermal efficiency of the thin-wall MEMS TE generator.

During operation, a fuel-air mixture flowed down the channel and burned on the catalyst. The selective deposition of the catalyst confined the reaction to the thermopile region. Most of the heat released was conducted laterally through the membrane and thermopile to the cold silicon substrate. We used the resistive heater to test the thermal efficiency of our device, as shown in Figure 15. The relatively low thermal efficiency of our device was due to several factors. This demonstration device used very thin SiGe layers to validate the models, resulting in comparatively large parasitic conduction through the membrane; later devices could improve the efficiency by increasing the SiGe film thickness. Also, the doping levels in our SiGe films were sub-optimal. Finally, the contacts used in these devices degraded rapidly at temperatures exceeding 400 ℃. Device efficiency improved rapidly at elevated temperatures because of improved SiGe properties at high temperatures.

Power generation was successfully demonstrated from combustion of hydrogen in air, despite low overall efficiencies. Figure 16 shows images of the cold and ignited generator, with buckling due to thermal expansion after ignition. Autothermal operation was achieved following initial power input from the start up heater. Figure 17 shows the power input from the start-up heater vs. thermopile voltage output during one sequence of ignition and autothermal operation for hydrogen combustion in air. A thermopile voltage was generated even with zero heater power, showing conversion of chemical to electrical energy. We have also demonstrated autothermal operation for ammonia and butane combustion in oxygen. The thin wall heat dissipation was too large and the catalyst area too small to allow for autothermal combustion of hydrocarbons in air.
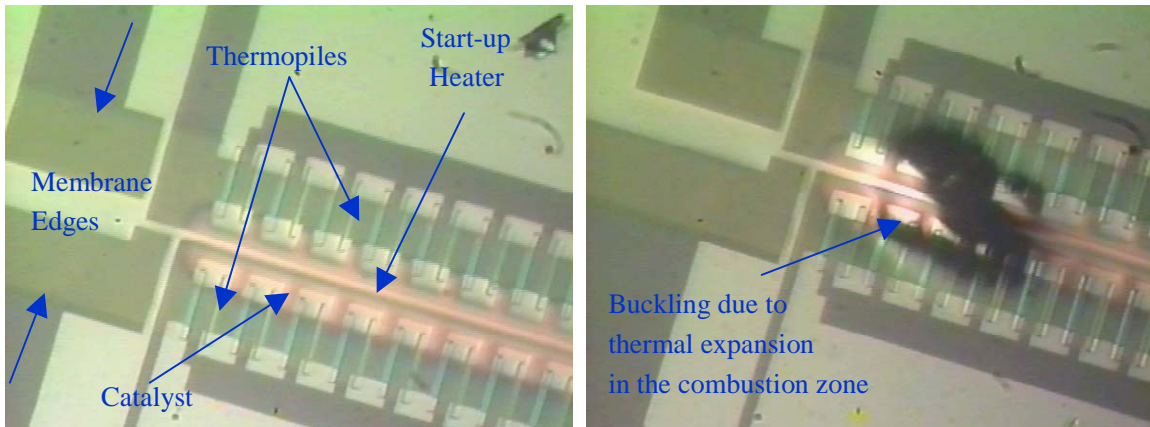
Figure 16. Top view of the cold and ignited TE generator

To realize the potential efficiency of this technology, several steps would be necessary. First, moving from the membrane type reactor (with high heat losses) to the suspended micro reactor structure (Section 2), would be key to drastically improve the thermal isolation of the hot reaction zone and thus improve the thermal efficiency of the generator. The main challenge to this would be to redesign the reactor to be essentially stress free at the hot/cold junction where the thermopiles connect the hot and cold zones. Such designs have been proposed, but the integration would be non-trivial. Another fundamental problem is stable, high-temperature contacts.

Although many exotic TE materials with high figures of merit have been and are being developed, they are almost exclusively limited to relatively low temperatures, rendering them useless for high efficiency system applications in our reactor. Additionally, if such materials are

not available at this institution, the device wafers would have to be sent to another place for trying out different fabrication steps. Therefore SiGe remains one of the best choices for further work, with a maximum projected efficiency of 5-6%. Because of this limited efficiency prospect, and the other challenges, it was decided to consider TPV power generation as an alternative direct power generation scheme.
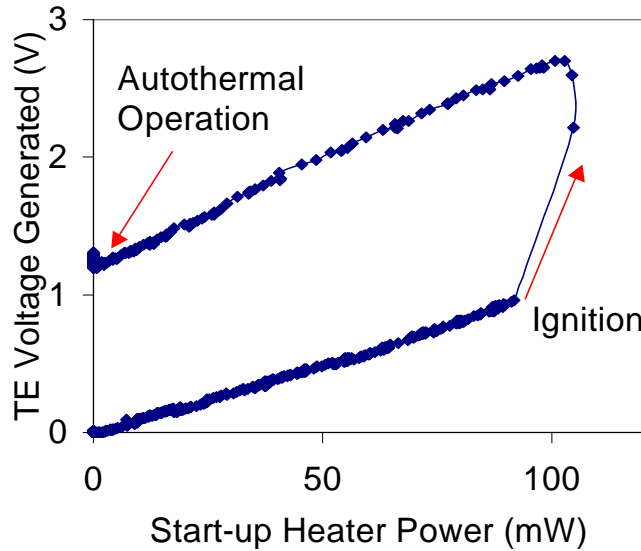
Figure 17. Autothermal operation and power generation in the thin-wall TE generator. An integrated heater is used to achieve ignition and is subsequently turned off.

3. MEMS THERMOPHOTOVOLTAIC POWER GENERATION

3.1 Micro TPV MEMS Design and Performance

There is no general agreement about the potential maximum possible efficiency of TPV systems. Different theoretical and/or semi-empirical calculations suggest that it is somewhere in the 20-35% range. Although these are encouraging numbers, it is currently more realistic to regard15% as an upper ceiling for the near future. The vehicle for the TPV effort was the suspended-tube micro reactor, which was very well suited for TPV purposes. Since there was no need for contact between the hot and the cold zones, there would be no stress related problems. There was also no heat conduction path between the hot and cold zones, other than the tubes of the reactor. So if the ensemble were vacuum packaged, radiation would account for almost all of the heat transfer, as desired. Although the best photocell materials are quite exotic and not readily available, they can be acquired separately and then integrated into the system. No fundamental process changes were necessary to the micro-reactor structure. Figure 18 is a conceptual schematic of the TPV generator.

We carried out TPV power generation experiments based on this concept. A schematic of the test-setup is shown in Figure 19. A 1wt. % Pt on La-doped γ-Al$_2$O$_3$ (Alcoa Ga-200LSF Alumina), reduced *ex-situ* in H$_2$ at 300˚C, was used as a combustion catalyst for these experiments. Energy conversion was achieved using one GaSb diffused junction photocell (purchased from JXCrystals

Inc.) placed about 1 mm from the emitter. This photocell was the best commercially available alternative for our application.
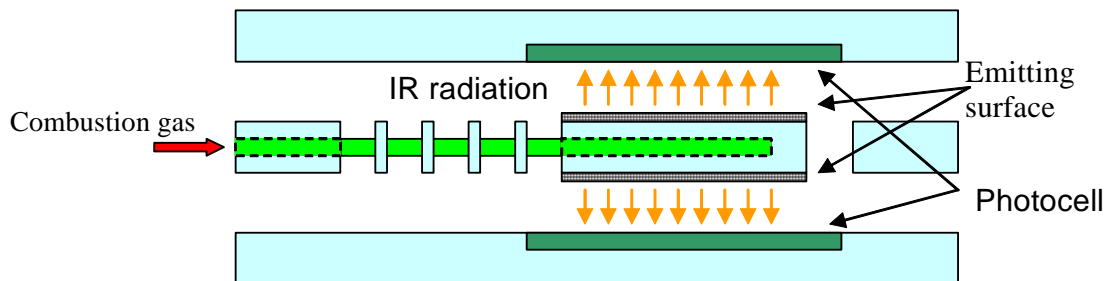
Figure 18. Schematic of a TPV generator.
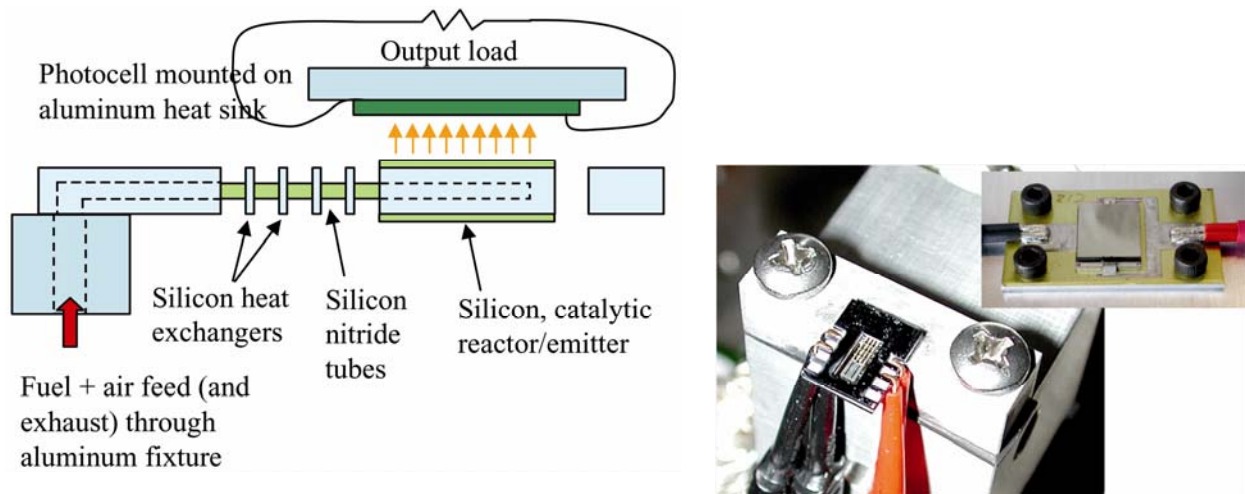
Figure 19. Schematic of the suspended-tube reactor in a TPV microgenerator configuration.

Mounted reactor and GaSb photocell.

Figure 20 shows the photocell output power and system efficiency as a function of emitter temperature. This was done using only electrical heating (no combustion) to better control the temperature. The graph clearly illustrates large performance improvements with increasing temperature

Autothermal combustion of propane in air was successfully achieved in the reactor. Figure 21 shows the propane combustion rate as a function of time. Initially, the propane and air flows are stable, and the temperature gradually increased with the electrical heater until ignition occurred. This transition was marked by a sharp increase in the combustion rate. After the reaction stabilizes, the electrical power was turned off, and the combustion continued autothermally, sustaining itself by the heat of reaction, with constant thermal emission at ~770˚C. Reproducible,

autothermal propane combustion was conducted for 2 hours before flow instabilities extinguished combustion.
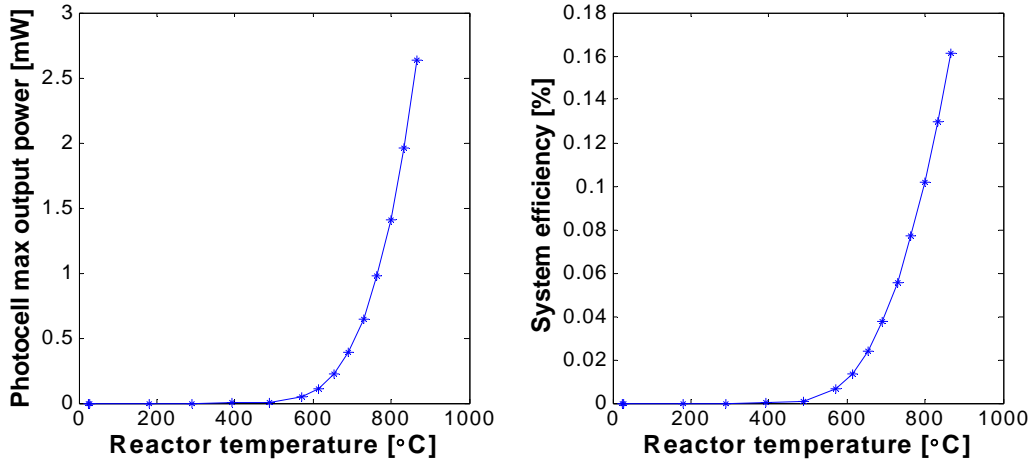
Figure 20. Photocell power output and system efficiency, as a function of temperature, during electrical heating of the reactor.
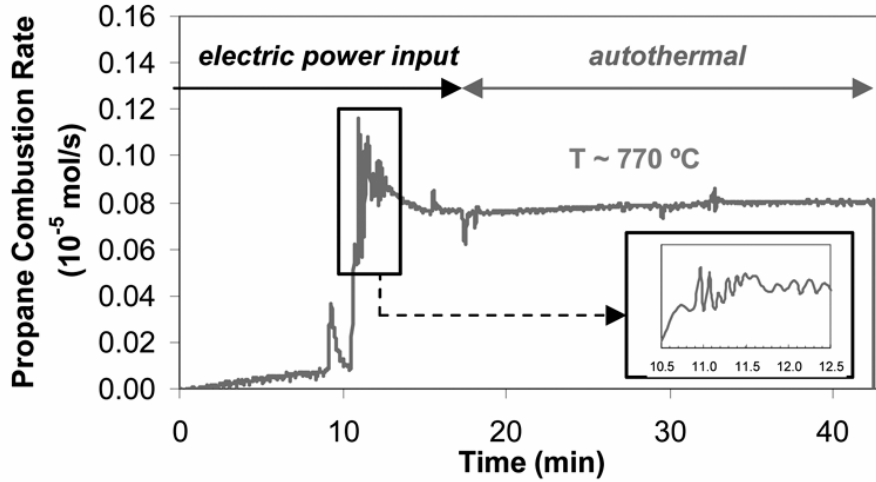
Figure 21. Stable and autothermal propane combustion in the reactor.

During autothermal combustion, the maximum output power of the photocell was 1.0 mW, which corresponds to a power density of 32 mW/cm^2. This constituted the first net electrical power generation in a MEMS device using TPV. The system efficiency, defined as the power output of the photocell divided by the thermal power released from the combustion, was 0.08%. These results are summarized in Table 3. Later tests under similar conditions yielded very similar results, confirming the repeatability of the experiment.

The recorded results are a proof of concept for the TPV microgenerator. Although power outputs and efficiencies are relatively low, they show promise for further improvements to the device operation. To illustrate this, Table 3 includes predictions based on three basic

modifications of the TPV microgenerator. First, using one photocell on each side of the reactor will double both the power and the efficiency. Second, vacuum packaging will eliminate heat losses to the air, increasing the radiative component of heat loss by a factor of three, thereby, according to experimental data, increasing the efficiency by a factor of three. Third, by using a conservative extrapolation of the curves in Figure 20 to a temperature of 1000°C, together with the two first improvements, we predict a power exceeding 16 mW, corresponding to a power density of 250 mW/cm^2, and an efficiency of more than 2.4%. This would bring both the power density and efficiency to about 25% of the project goals of 1 W/cm^2 and 10%.

Table 3. Data and predictions for TPV power generation during autothermal combustion in the suspended-tube reactor.

Fuel (Propane)	
Flow rate	2 mL/min
Air flow rate	47.6 mL/min (stoichiometric)
Catalyst	1 wt.% Pt – Al$_2$O$_3$
Conversion	46 %
Combustion power	1.3 W
Reactor	
Temperature	770°C
Electrical power input	0 W
GaSb photocell	
Power output	1.0 mW
Power density	32 mW/cm^2
System efficiency[*]	0.08 %
Projections for 2 photocells, in vacuum, at 1000°C	
Power output	> 16 mW
Power density	> 250 mW/cm^2
System efficiency[*]	> 2.4 %

Higher temperature is critical to increased TPV performance. The silicon nitride covered silicon reactor can be approximated as a grey-body of emissivity measured by one test to be approximately 0.7. Figure 22 shows the corresponding emission spectrum at 770°C (the temperature we achieved during combustion) and 1000°C. Since only photons of energy higher than the photocell band gap can be transformed into electric power, it is clear that not only higher temperature is desirable, but also a photocell material with lower band gap than GaSb. Because of the limitations of the reactor material (silicon), the emitter temperature cannot exceed 1000-

1200°C. This should, however, with appropriate photocells, be hot enough to achieve the power densities desired. In this temperature range, a photocell band gap of 0.4-0.5 eV would probably be best suited.
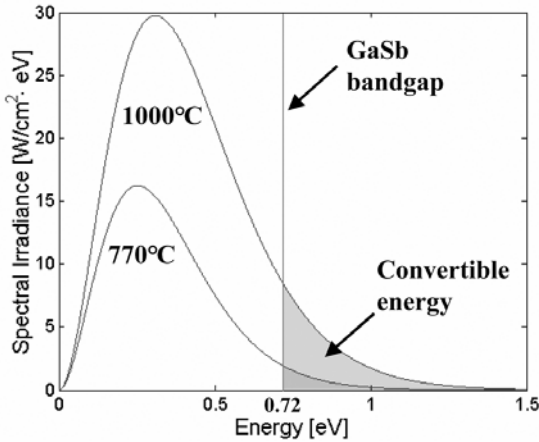
Figure 22. Power radiation spectrum as a function of photon energy for a greybody of emissivity 0.7 at 770°C and 1000°C.

3.2 Micro-Fuel Combustor Improvements

Three different efforts were implemented to improve the TPV microgenerator: fabrication of a new suspended-tube reactor design (version 2), building of a new test setup for the new devices, and development of a completely new tube fabrication process (reactor version 3).

The major difference of version from the old design was the increased surface area. The old design had an emitter (reaction) zone measuring 1.5mm x 2.5mm, whereas version2 had 5mm x 5mm. This would increase the overall power of the generator, since power is proportional to area. The larger size furthermore made it simpler to test with photocells on *both* sides. The new process was on 6-inch silicon wafers (4-inch before), and the extra thickness of the wafers, with the larger area, would give a much larger reaction volume allowing higher temperatures during combustion. To support the much larger reactor, the new design had 8 instead of 4 suspended silicon nitride tubes. Figure 23 shows images of the masks of the version 2 design to illustrate the flexibility in design of the fuel processor.

We developed a new set-up which addressed short comings in the original set up. First, automation of the test was implemented with a computer running Labview. The program gathered test data about the suspended-tube reactor, converting the data real-time into useful information such as reactor temperature and input power. It furthermore traced I-V characteristics for two photocells at each test point, and extracted the maximum output power directly. This allowed a better understanding of performance during testing. Chemical data was already automated with a mass spectrometer, but since it cannot be run by the same software, the two data sets must be compared after testing. The remaining task is to design a new aluminum fixture for the larger devices. Finally, new heat sinks were made for the photocells, and these include water cooling rather than forced air convection. This allows cooling of the cells without affecting the ambient around the micro-reactor.

In fabricating version 2 of the suspended-tube micro-reactor, several fabrication problems were encountered. Switching to a six-inch process (as required by our fabrication facility), while allowing more devices per wafer, presented increased non-uniformity problems, especially in the Deep Reactive Ion Etcher (DRIE). While such problems were addressed successfully in the past, we decided to start a parallel design effort (version 3) that would eliminate the uniformity issues. The result was a completely new way of fabricating the tubes.
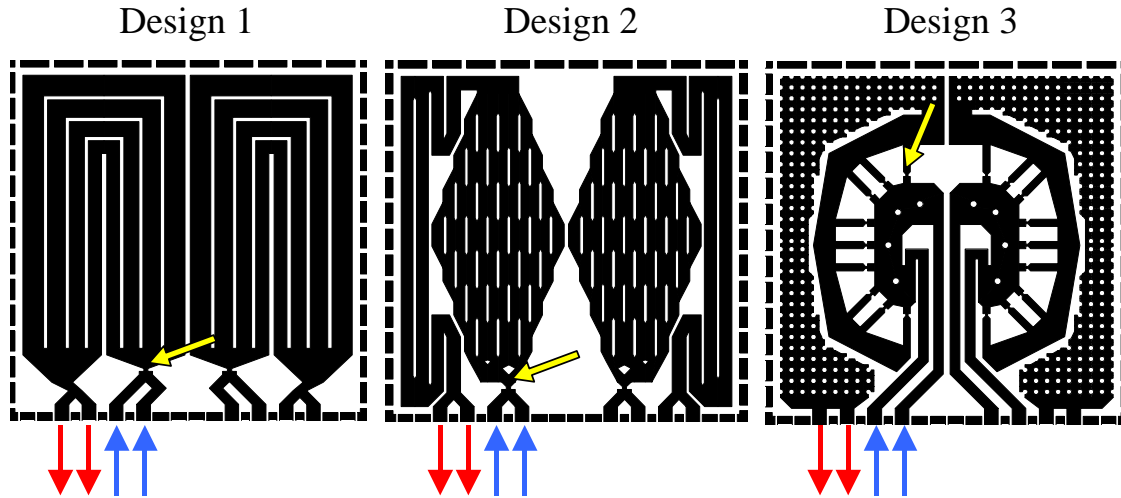
Figure 23. Examples of version 2 reaction chamber designs. The black areas are the etched chambers/channels. Design 1: simple parallel channels with matched flow resistances Design 2: an expanding reaction chamber for the gas to see an increasing amount of catalyst as it proceeds through the reactor. Design 3: spread out catalyst to improve combustion uniformity. The yellow block arrows indicate where the gases first see catalyst (only 1 of the 9 spots is indicated by an arrow in Design 3).

The old process relied on the mold for the tubes being etched in the plane of the wafer. This yielded rectangular tubes, typically with defects at the corners due to etch artifacts in the DRIE. In version 3, the molds for the tubes were etched vertically through the wafer, allowing circular cross-sections. This in itself yields stronger tubes. Furthermore, since it was done with a through-etch, the corner artifacts were eliminated. A simple schematic of the concept is shown in Figure 24. In addition to the structural strength advantages of this process, it also eliminated the need for SOI and ultra-thin wafers, which were used in the old process and are quite expensive. This effort is continuing under sponsorship by the MURI (See Section 7). Several process optimizations were performed and we are close to having a new prototype for test in both fuel processing and TPV.

Gas flow **Silicon nitride tubes**

Silicon heat exchangers

g
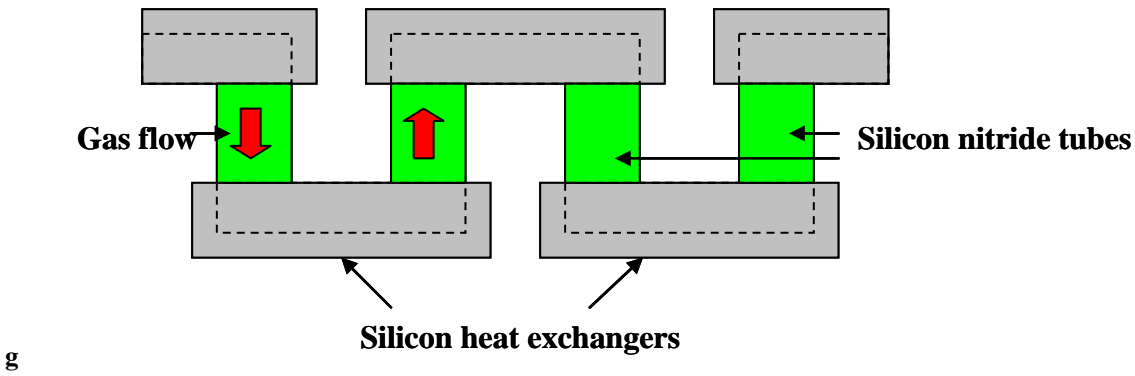
Figure 24. Suspended tube reactor version 3 tube design. Etching circular molds in the center sacrificial wafer allows fabrication of silicon nitride tubes of circular cross-section. The schematic shows one meandering tube. There are 8 more in parallel into the page, all connected by the silicon heat exchangers.

4. MEMS PALLADIUM HYDGROGEN PURIFIERS
4.1 Supported Pd Membrane Devices

High hydrogen purity is required in a variety of processes, from the microelectronics industry to PEM fuel cells. For portable-power applications, it is desirable to produce hydrogen in-line via fuel reforming, either of hydrocarbons or ammonia. However, byproducts and reactants may irreversibly damage fuel cell performance. For these reasons, it is of interest to develop an intermediate hydrogen purification unit capable of extracting hydrogen from a feed stream containing CO, CO_2 or NH_3 (i.e., fuel reformer effluent). MIT palladium micromembranes have been shown capable of hydrogen purification at high fluxes and high selectivity. Palladium micromembranes, shown in Figure 25, consist of a free-standing Si_3N_4/SiO_2 support upon which an adhesion metal (10 nm Ti) is deposited, followed by 200 nm of Pd or Pd-based alloy. Perforations of ~ 4μm in diameter are then etched through the support to expose the Pd film. The resulting hydrogen purification device is intended as an intermediate stage between hydrogen generation and the fuel cell stages.

Pictures courtesy of Felice Frenkel
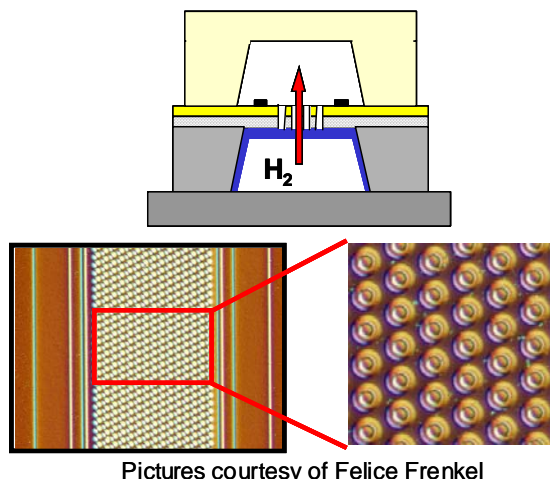
Figure 25. MIT Palladium micromembranes

Both pure Pd and 23% Ag-Pd films were fabricated. The latter was achieved via depositing alternating layers of pure Ag and Pd, in appropriate relative thicknesses to achieve the desired average alloy composition. Auger analysis of films, both as-fabricated and after simulating operating conditions for one hour (350°C under N_2), indicated that while variations in composition occur across the film depth, desired alloy composition was achieved within +/- 15% throughout the 200 nm film (Figure 26).

We experienced problems with Pd membrane deactivation (Figure 27). We used a sputtering Auger test apparatus to obtain composition data of the surfaces of our membrane films as well as depth concentration profiles. These results suggested that exposure to reducing atmospheres deactivated the membranes and elevation of the temperature accelerated this deactivation. Deactivation was not caused by a massive interdiffusion of various membrane layers, as the Pd/Ta/SiO_2 films maintain their layer-by-layer structure, within the resolution of the instrument.
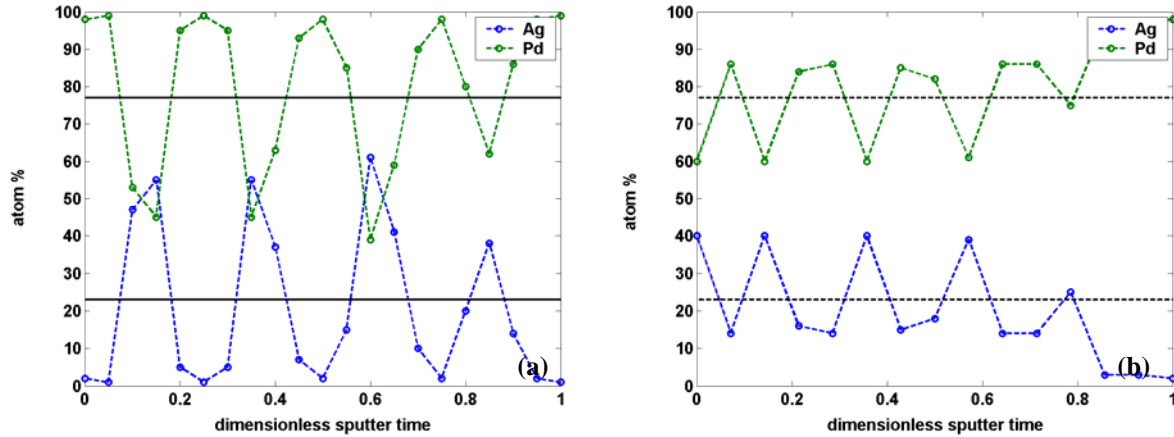
Figure 26: Auger analysis of electron-beam deposited Ag-Pd films via alternating pure layers; (a) upon fabrication, and (b) after simulating operating conditions at 350°C under N_2.
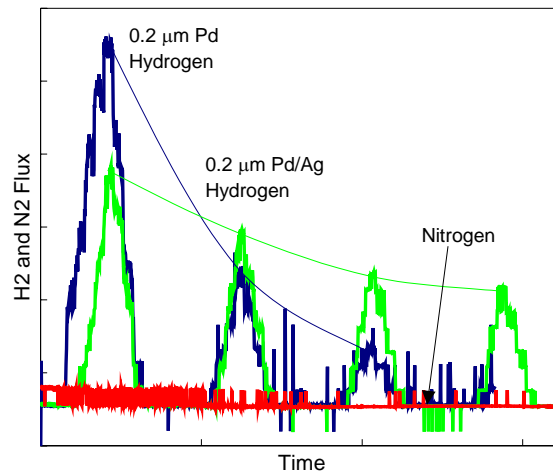
Figure 27: Decrease in H2 permeation in Pd and Pd/Ag alloy membranes during temperature cycle programs.

We also tested devices with different adhesion layers, to empirically determine if the adhesion layer played a strong role in membrane deactivation. Figure 28 shows a comparison of normalized hydrogen fluxes for membranes with Ti and Ta adhesion layers. Clearly a dramatic difference was observed in deactivation behavior.

Fabrication procedures were modified to ensure greater purity and uniformity of metal films during deposition, and to prevent accumulation of debris on device surfaces during die sawing of wafers into individual chips. These modifications resulted in a stable hydrogen flow through the membrane over long operating times, with H_2-Ar selectivities greater than 1000:1. In addition, hydrogen molar fluxes of ~3 mol/m^2/s were achieved, which is an order-of-magnitude improvement over comparable macroscale systems.

The final fabrication process is illustrated in Figure 29. The completed microdevice was comprised of two layers, each contained one flow channel. The first, or primary, layer contained the feed flow channel, membrane support with resistive heaters and temperature sensors, and the active film. The second, or packaging, layer contained the sweep flow channel, with lateral exposures to allow access to electrical contacts on the underlying primary layer. The completed layers are pictured in Figure 30, with feed and sweep flow channels facing downward.
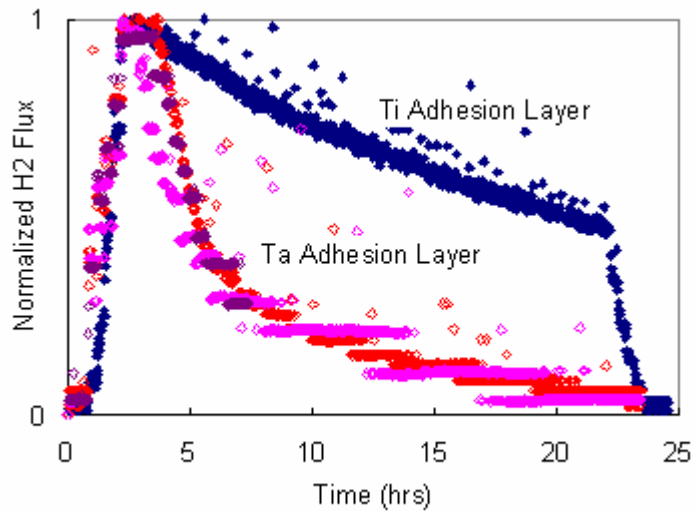
Figure 28: Effect of Ti and TA adhesion layer on membrane deactivation rates

For the primary layer, fabrication begins with a double-side polished (DSP) 150 mm single crystal (100) silicon substrate. Thermal oxide is grown to a thickness of 250 nm and subsequently coated with a 300 nm film of stoichiometric silicon nitride (Si_xN_y) via low-pressure chemical vapor deposition (LPCVD). A hard-mask for the feed flow channel was patterned in the backside using standard photolithography followed by dry etching of the nitride film with SF_6 and oxide removal using standard buffered oxide etch (BOE) solution of HF and NH_4F. The membrane pore structure, comprised of two regular arrays of 4 micron diameter holes, is patterned in the front-side nitride film using photolithography followed by dry SF_6 etching, keeping the underlying oxide layer intact. An electron-beam deposited Ta-Pt-Ta (10:200:20 nm) metal layer was patterned via standard lift-off process to form temperature sensing resistors and heaters. The initial tantalum film provided strong chemical adhesion with the nitride surface, while the final

film helped to prevent agglomeration of the primary platinum metal at high temperatures. The wafer was subsequently loaded into a Teflon holder that protected the front-side metallization, then submerged in an aqueous 20 weight % KOH bath at 80^oC until the feed flow channel was formed, and the membrane support fully released, typically ~ 8 hours. A post-KOH etch cleaning step was followed by annealing of the heater metallization at 650^oC under nitrogen for one hour. At this point, the device wafer was ready for deposition of the active metal film. Deposition, employed a thin (10 nm) layer of titanium to provide strong chemical adhesion between the silicon oxide and palladium films. For the silver-palladium alloy film, alternating thin layers of palladium (29.8 nm) and silver (12.9 nm) were deposited, such that the outermost layers were palladium, and selection of the appropriate layer thicknesses to achieve the desired composition of 23 wt% silver. Significant interdiffusion yielded a palladium composition greater than 40 weight-% throughout the film, with large local variations in alloy composition corresponding to individually deposited layers. Annealing at 350^oC for one hour, simulating typical operating conditions, reduced these variations to within +/- 15% of the desired composition at any given film depth. Thus, this procedure provided a fast, relatively inexpensive alternative to co-sputtering for thin alloyed films.
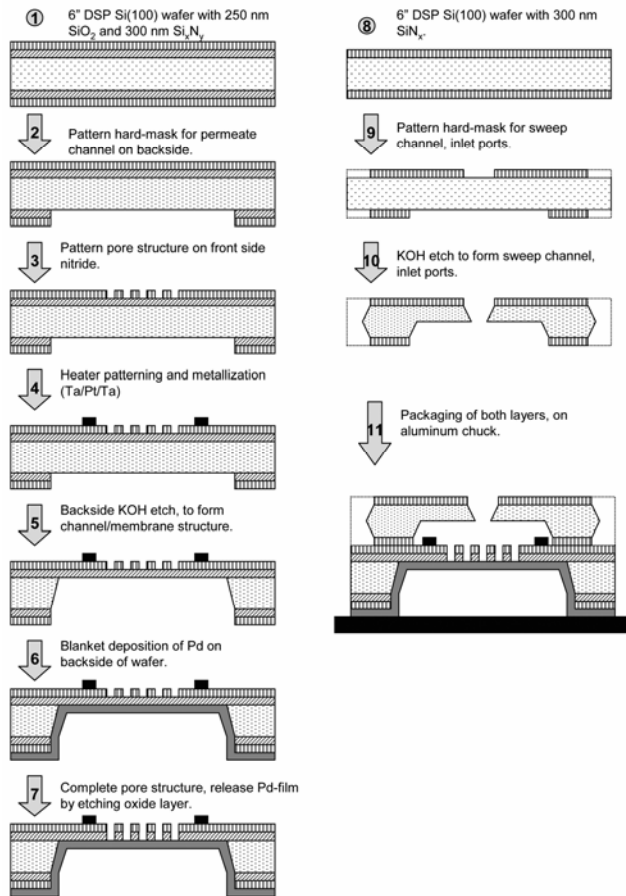
Figure 29: Fabrication process for primary and secondary microdevice layers.
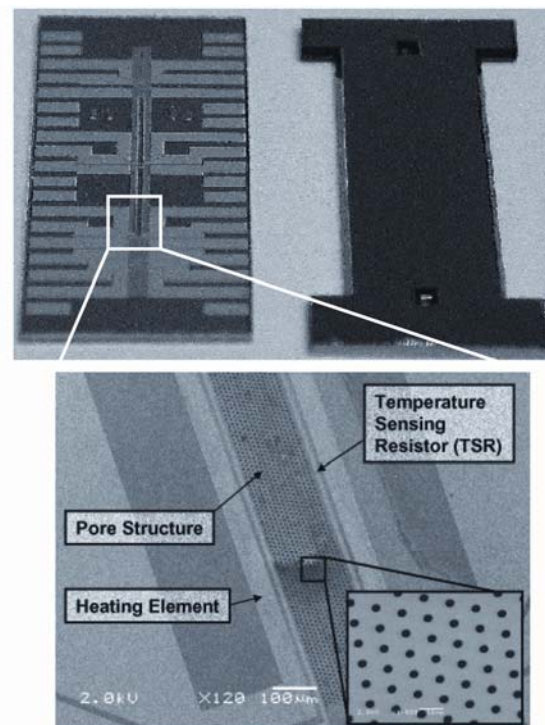
Figure 30: Picture of fabricated microdevice layers prior to packaging, with SEM image of temperature sensing resistor, heating element and membrane pore structure (inset).

The final step in fabricating the primary device layer was the release of the active film by patterning the pore structure through the membrane oxide film via BOE wet etches. Immediately after this step, a thin layer of photoresist was airbrushed onto the front-side of the wafer. The wafer was then mounted on an adhesive tape and cut into individual 8 x 16 mm devices, or chips, using a die sawing machine. The resist layer prevented accumulation of particles within the pore structure during the cutting process, as well as minimizing atmospheric exposure during handling and storage.

The packaging layer was fabricated from a second double-side polished 150 mm silicon (100) wafer. Low-stress silicon nitride (SiN_x) was deposited at a thickness of 300 nm. Hard masks for gas ports and sweep gas flow channel wee patterned into the front-side and backside nitride films, respectively, via standard photolithography and dry SF_6 etching. Lateral exposures were patterned on both sides of the wafer to provide access to electrical contacts on the underlying primary layer after packaging of the device. The wafer was immersed in a KOH bath, as described above, until flow channels and inlet ports connect midway through the wafer, forming the sweep flow channel (~ 4 hours). Lastly, the wafer is mounted onto an adhesive tape and cut into individual 8x16 mm chips using the die sawing machine.

Given the earlier difficulties with membrane stability, the first goal of the new device was to demonstrate the long-term stability and performance of palladium-film microdevices under ideal conditions. Experiments were performed at steady-state conditions using fixed sweep and feed flow rates of 10 sccm each, with a feed composition of 10% hydrogen, and an operating temperature of 350^oC. Hydrogen fluxes of 3-4 mol/m^2/s with average selectivities of ~ 1000:1 were obtained for both pure palladium and 23 wt% silver-palladium alloy films of 0.2 micron thickness. These fluxes corresponded to a sweep hydrogen concentration of 0.5%, and therefore a H_2 driving force of 9.6 kPa. These values were maintained over a prolonged period of time (> 10 hours) with no significant decrease in performance. The hydrogen flux achieved with the 23 wt% silver-palladium film was greater than that for pure palladium, as is consistent with trends reported elsewhere, and is an order-of-magnitude greater than values reported for free-standing 1 micron silver-palladium films employed in similar microdevices.

The chemical resistance of the palladium-based micromembranes to ammonia, carbon monoxide and carbon dioxide was also tested, to further determine device applicability as part of an integrated portable-power system. Experiments were performed using both pure and 23 wt% silver-alloyed palladium films to determine their chemical resistance to ammonia exposure. The catalytic cracking of ammonia has been demonstrated as a promising in-line source of hydrogen for portable-power systems (see Section 2). Upon exposure to 4% NH_3 / 86% Ar / 10% H_2 composition for ~110 minutes, no loss in hydrogen permeability was observed for pure Pd films. For the silver-alloyed film, a ~ 12% reduction in overall hydrogen flux was observed, of which half was recovered upon removal of the ammonia. The rapid, partially reversible nature of performance loss suggested a mild competitive adsorption. In both cases, the micromembrane devices were able to maintain high hydrogen fluxes both during and after exposure to an ammonia-contaminated hydrogen stream, thus indicating their usefulness in an integrated portable-power system employing a catalytic cracking stage for hydrogen generation from ammonia fuel.

Additional experiments were performed to study the chemical resistance of both pure and silver-alloyed palladium films to carbon dioxide and carbon monoxide, both common contaminants produced from hydrocarbon reforming schemes. The performance of pure and

silver-alloyed palladium films exposed to carbon dioxide showed no significant change. Hydrogen flux performance before, during, and after exposure to carbon monoxide was also investigated. For the pure palladium device, a rapid decrease in flux to ~ 40% of steady-state occurs upon exposure. When carbon monoxide was removed from the feed, hydrogen flux rapidly recovered to ~ 70% of initial steady-state flux. For the silver-alloyed film, introduction of carbon monoxide to the feed resulted in a gradual decrease in performance. After ~ 7 hrs exposure, hydrogen flux wasreduced to 60% of the initial steady-state value. Removal of the contaminant resulted in gradual recovery of hydrogen permeation to ~ 90% of the initial steady-state value, over ~ 100 min period. Despite a ~ 40% reduction in hydrogen flux for 23 wt% silver-palladium films, hydrogen fluxes achieved were still a four-fold improvement over 1 micron films and an order-of-magnitude greater than those reported for conventional membranes, while maintaining high selectivity (~1000:1). For these reasons, the present microdevice should be compatible with hydrocarbon reforming for hydrogen generation.

4.2 <u>Self-supported Pd Membrane Tubes</u>

We also explored the ability of MEMS fabrication to achieve higher active area membrane structures. The rationale behind typical palladium membrane design was that in order for a thin palladium membrane to survive large pressure gradients, it had to be supported by a thicker, porous structural layer. The mechanical and selective functionalities of the membrane were thus decoupled. However, this decoupling resulted in a smaller effective palladium membrane area. If palladium membrane tubes could be fabricated of sufficiently small diameters, even very thin walled tubes could withstand large pressure gradients. The large resistance to flow in small diameter tubes could be circumvented by fabricating a large number of short tubes accessed in parallel by a manifold.

Figure 31 shows the fabrication process flow devised for fabricating all Pd tube membranes. A low-stress silicon nitride coated wafer was patterned on the back and etched to leave free standing nitride membranes. Then palladium was deposited and patterned using lift-off on the front side. Subsequently, patterned thick resist was used as a sacrificial layer for tube formation. The thick resist was coated with a blanket layer of palladium. The nitride membranes were removed from the back side using a dry etch, and the sacrificial photoresist was removed from the channel using solvents and a one-sided etch jig. The resulting tube should have a diameter of about 10 microns and a high hydrogen permeation rate. Self-supporting Pd membrane tubes were fabricated using the procedure. Moreover, corrugated surface features were incorporated into the Pd membrane structure by photolithographic patterning of the sacrificial resist layer. Structures (Figure 32) were smooth, and local buckling was not observed. However, after SiN and photoresist removal, the top layer of Pd separated from the bottom Pd layer. Solutions to this fabrication problem were investigated, but given the successful realization of long-term stability of the original membranes, we chose to focus on those.

1. Initial wafer coated with SiN_x
2. Etch with KOH through wafer to SiN_x

3. Coat and pattern negative resist
4. Deposit 0.2 μm of Pd, lift-off

6. Coat and pattern thick resist (10 μm)
7. Deposition of Pd (0.2 μm)

8. Remove back side nitride
9. Remove resist with acetone
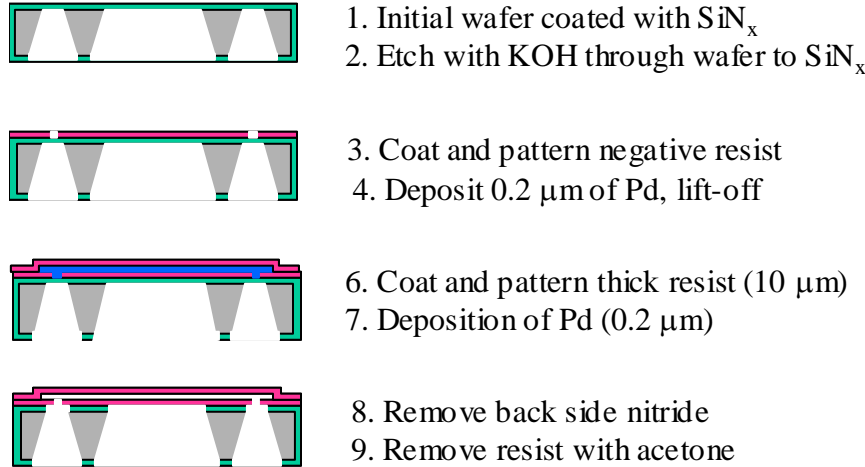
Figure 31: Fabrication process for self-supported Pd tube membranes
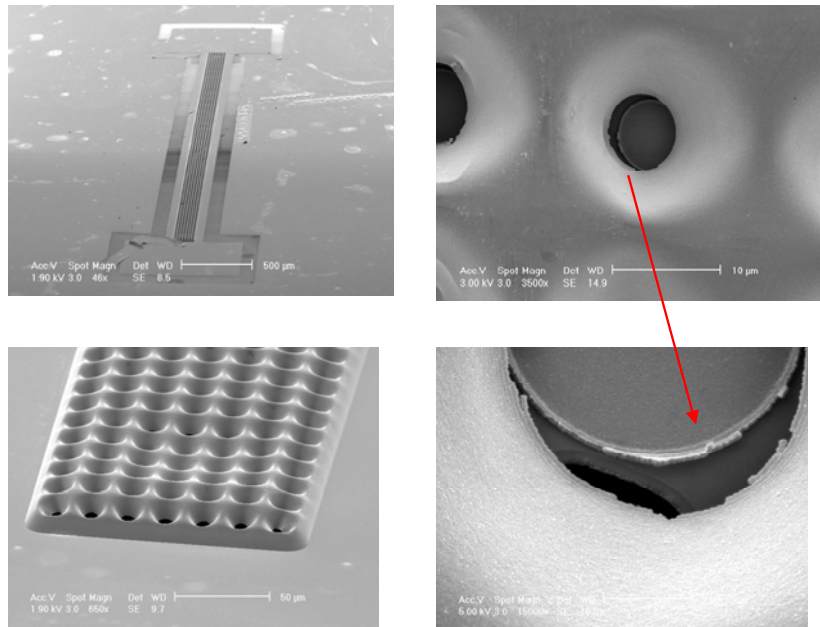
Figure 32: Self-supporting Pd tube membrane test structure

5. SYSTEM ISSUES

5.1 <u>Evaluation of energy generation schemes</u>

Ultimately, the performance of the developed fuel processors have to be evaluated and compared in terms of overall power generation efficiency, reliability, and safety. As a step towards this effort we evaluated different energy generation schemes. The microgenerator must possess three critical characteristics in order for small, fuel-based power supplies to successfully compete with batteries. First, the generator must result in a substantial improvement in energy density over batteries to compete with the established technology. Second, the generator must be

as efficient as possible to reduce device heating. Third, the generator must be robust, to be broadly applicable in real-world environments.

The energy density of a power supply determines device run time for a given power supply mass or volume. We chose to evaluate power density both on a mass and volume basis. Mass considerations are primarily of importance to Department of Defense (DoD) needs while volumetric energy density (form factor restrictions) appear to be a critical consideration in commercial applications such as laptop computers and cellular telephones. The volume vs. mass energy density distinction is critical for microgenerator developers, since on a volume basis fuels hold a significantly smaller edge over batteries. While chemical fuels are up to 100 times as energy dense on mass basis, fuels are at best able to boast only ~25 times the energy density on a volumetric basis.

Different micro-generation approaches were compared by using broadly accepted system efficiencies and making simple assumptions about the technology, without any system specific knowledge, except for case involving our microgenerator. Most generally, a power supply energy density (E_{ps}) can be calculated using:

$$E_{ps} = E_{fuel} \times G_{eff} \times F_{fuel}$$

where E_{fuel} is the energy density of the fuel, G_{eff} is the generator efficiency and F_{fuel} is the fuel fraction of the power supply. Assuming for the sake of comparison that all generators could be miniaturized to roughly half the power supply volume and mass, the generator efficiency and the energy density of the fuel determines power supply performance.[1] The results of our analysis are summarized in Table 4.

Efficiency is an important factor in determining supply energy density, but it is even more critical because of heat management. Generator efficiency determines what fraction of the chemical energy in the fuel is converted to electricity and what fraction is converted to heat. Batteries discharge electricity with 80-90% efficiency. Even a highly efficient fuel cell system will operate near 50% efficiency, and therefore the electronic device using a fuel based power supply has to dissipate more heat than when running on batteries. It is therefore the system efficiency that determines the degree to which a device will have to heat up in order to dissipate the excess heat, and not the operating temperature of the generator.

---

[1]   The assumption of a constant size across all technologies is conservative for this analysis. Since chemical reaction rates scale exponentially in temperature, higher temperature systems are substantially smaller than their low temperature counterparts for a given power level. The smaller size of the high temperature generator results in a higher F_{fuel}, and so a larger comparative E_{ps}.

Table 4: **Evaluation of different micropower generation schemes**

Technology	E_{fuel}(vol)	E_{fuel}(mass)	G_{eff}	F_{fuel}	Performance Criteria			
					E_{ps}(vol)	E_{ps}(mass)	Heat Load	Complexity
Li-Ion Batteries					330	140	1.2 W	Low
Carnot Engines	*7,878	13,750	10%	50%	395	690	10 W	Low
Fuel Cells:								
DMFC	^1,777	1,899	35%	50%	310	330	3 W	High
PEM/Hydride	#2,382	794	50%	50%	600	200	2 W	Low
PEM/MeOH	‡3,450	4,051	&30%	35%	360	425	3.3 W	High
PEM/NH$_3$	3,105	5,175	40%	50%	620	1,035	2.5 W	Moderate
Butane µSOFC	7,878	13,750	50%	50%	1,970	3,440	2 W	Moderate

* Butane
# Solid hydride (2% hydrogen by weight, 50% porous
‡ 1:1 methanol:water mixture
^ 3:7 methanol:water mixture
& Estimate including evaporation but not CO clean up

E (vol): Wh/L
E (mass): Wh/kg

Fuel cells are by far the most efficient generators, at 30-60%. Unfortunately, micro fuel cells have been severely limited by the type of fuel they can process – primarily hydrogen. A methanol reformers reacts a mixture of methanol and at least 50% water at 200-400 °C. The reformer/PEM system takes a size penalty (smaller F_{fuel}) relative to PEM/Hydride because of the addition of the reformer to the generator. The system efficiency is also reduced because of the efficiency losses associated with CO clean-up. Methanol is also sufficiently reactive for direct use in a fuel cell with the aid of expensive catalysts, but it is a partially oxidized hydrocarbon, and therefore starts with a lower energy density than other fuels. In addition, direct methanol fuel cells (DMFCs) can only utilize methanol that is substantially diluted with water, at best down to about 30% of the initial energy content. (Most current systems operate on methanol diluted to only a few percent in water, as higher concentrations dissolve the polymer fuel cell membrane or increase cross-over). DMFCs also operate at the lower end of the fuel cell efficiency spectrum, resulting in systems that at best will match battery volumetric energy density.

Various Carnot-limited thermal power generation schemes could be miniaturized, such as the thermoelectric and thermophotovoltaic approaches discussed in Sections 3 and 4. Our combustion-based approaches rely on high-energy, simple hydrocarbon fuels. The lower efficiencies in these types of systems are offset by the simplicity and robustness of the devices. It appears that high energy density micro power generators will have to be based on dense, common and inexpensive hydrocarbon fuels combined with efficient fuel cell technology. The need to clean up the hydrogen for use in a PEM fuel cell adds considerable complexity and volume to the power generator. On the other hand solid oxide fuel cells (SOFCs) are as efficient as PEM fuel cells and can operate on mixtures of hydrogen, carbon monoxide, and residual unconverted hydrocarbons – the products from partial oxidation. However, there has been limited development of microfabricated SOFCs to date.

As a result of the above analysis, we proposed and were granted a MURI from the Army Research Office to develop the knowledgebase for micro SOFCs integrated with microgenerators such as those being developed as part of this DARPA program (see Section 7).

5.2 **System component evaluation**

Use of components, such as pumps and valves, needs to be minimized since feedback of electrical energy to the processor results in a large efficiency loss. Moreover, the same components are also likely to be the only elements of the system with moving parts, which raises potential reliability issues. Based on experimental data from the different power generation schemes and component performance characteristics, we have evaluated different designs options for the fuel processing system. For example, pressure gradients in the fuel processor are necessary to achieve flow, and can be achieved either using micropumps, or a pressurized fuel source. Liquid fuels, although desirable, are not easily pressurized. Although promising micropump development efforts are under way in related efforts, energy efficiency of these devices is likely to be low.

Driven by the need for a fuel-air delivery system with low electrical power dissipation for any microgenerator system, the possibility for using jet pumps was investigated. The both mechanically and electrically passive nature of the jet pump made it an apparently appealing choice. The combined requirements of low flow rates and high aspiration ratios (and hence high-velocity jets) necessitated using microscale geometries. Since there was no literature available on the miniaturization of jet pumps, a feasibility study was carried out. The details of this study are presented in Section 6.3).

The requirements for the air-fuel delivery system vary depending on the fuel gas used. Eventually the system should be running on hydrocarbons such as propane or butane, which require mass aspiration ratios of about 10 and 18 respectively, with air. To achieve high energy densities in the system, atmospheric air must be used. Also, it was estimated that the pump would have to work against an internal system pressure of about 0.2 psi (1333 Pa) in excess of atmospheric pressure. The flow rate should be on the order of a few sccm (standard cubic centimeters per minute). The ideal jet pump approximation (an upper limit to the pump performance) allows a relatively simple solution to the mass aspiration ratio as a function of area ratio, jet velocity and outlet pressure. For any jet velocity, there is an optimal area ratio. It also shows that the energy needed to overcome the backpressure can only come from increasing the jet velocity. This analysis showed that for subsonic flow (lower than about 300 m/s), the aspiration requirements for butane are far from being met, and those for propane seem unlikely. As a consequence, it is necessary, even for the ideal jet pump, to go to supersonic flow.

To get an idea of the dimensions needed for the microgenerator jet pump, we assumed that the generator was running on butane. The simulations showed that for practically any application of jet pumps in microgenerators, the flow would be laminar, which proved to be the main problem for microfabricated jet pumps. The moment the flow in the jet pump becomes laminar, viscous friction severely compromises the achievable aspiration ratio.

The conclusion of computational fluid dynamics simulations and experiments (Figure 33) is that if it is already hard to make ideal jet pumps perform well enough, there is little hope for microscale (laminar flow) jet pumps. Even if supersonic nozzles are employed, the flow is likely to remain laminar, and the performance is much worse than that of the ideal case. The only approach we can foresee is to modify the flow to approach that of an ideal jet pump. A possible procedure to realize this was proposed based on arrays of many smaller nozzles, as opposed to one single nozzle. Simulations suggested that the aspiration ratio would only be about 15% less

than that of the ideal jet pump – a considerable improvement, but probably not sufficient to justify further developments.
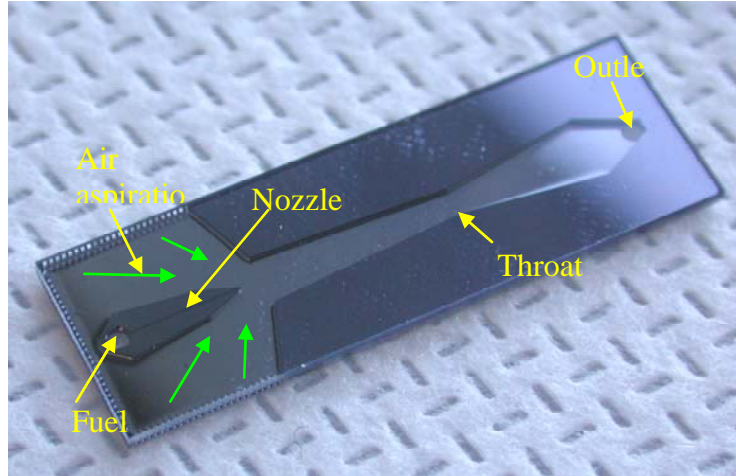

Figure 33: A microfabricated prototype jet-pump

6. PROGRAM TRANSITIONS

Aleks Franz and Samuel Schaevitz, a postdoc and PhD student, respectively, in the MIT DARPA MEMS project, licensed the MEMS suspended-tube reactor/heat exchanger developed in this program (Section 2) to start a new company, Lilliputian Systems Inc. This ~3 year old company successfully transferred the fabrication and testing of the MIT suspended-tube reactor/heat exchanger. The company aims to combine the hydrogen reforming concepts of the DARPA program with microfabricated solid oxide fuell cells (SOFCs) into an integrated, portable fuel-to-electrical power generator. The company received ATP funding and successfully completed several rounds of financing.

Based on the device work done in the MEMS DARPA program, the Principal investigator and a team of MIT faculty proposed and were granted a MURI from the Army Research Office to develop the knowledgebase for microchemical systems for conversions of fuels to electrical energy. This MURI continues to investigate thermally efficient MEMS based systems for fuel processing and Pd purification systems along with micro SOFCs.

7. PUBLICATIONS AND CONFERENCE PRESENTATIONS

7.1 Publications:

1. S. B. Schaevitz, A. J. Franz, K. F. Jensen, and M. A. Schmidt, "A Combustion-Based MEMS Thermoelectric Power Generator," Transducers '01 Munich, Germany, June 2001.

2. L. R. Arana, S. B. Schaevitz, A. J. Franz, K. F. Jensen, and M. A. Schmidt, "A Microfabricated Suspended-Tube Chemical Reactor for Fuel Processing," in *Proceedings of*

the Fifteenth IEEE International Conference on MicroElectroMechanical Systems, IEEE, New York, pp. 212-215

3. L.R. Arana, S.B. Schaevitz, A.J. Franz, K.F. Jensen, M.A. Schmidt, "A suspended tube microreactor for thermally efficient fuel processing," in *Proceedings of the Sixth International Conference on Microreaction Technolog*y, AIChE New York, pp. 147-155 (2002)

4. L.R. Arana, S.B. Schaevitz, A.J. Franz, M.A. Schmidt, K.F. Jensen. "A Microfabricated Suspended-Tube Chemical Reactor for Thermally-Efficient Fuel Processing," *the Journal of Microelectromechanical Systems (JMEMS)* **12** 600-612 (2003)

5. O.M Nielsen, L.R. Arana, C.D. Baertsch, M.A. Schmidt, and K.F. Jensen, "A Thermophotovoltaic Micro-Generator for Portable Power Applications," TRANSDUCERS, Solid-State Sensors, Actuators and Microsystems, 12th International Conference on, 2003 ,Volume: 2 , 8-12 June 2003 June 2003, pp.714-17.

6. L.R Arana, C.D Baertsch, M.A Schmidt, and K.F .Jensen, "Combustion-assisted hydrogen production in a high-temperature chemical reactor/heat exchanger for portable fuel cell applications, "TRANSDUCERS, Solid-State Sensors, Actuators and Microsystems, 12th International Conference on, 2003 ,Volume: 2 , 8-12 June 2003 pp1734 - 1737 vol.2

7. B. A. Wilhite, M. A. Schmidt and K. F. Jensen, "Palladium-based micromembranes for hydrogen separation: device performance and chemical stability," *Ind. & Eng. Chem. Research* **43**, 7083-7091 (2004)

8. L.R. Arana, C.D. Baertsch, M.A. Schmidt, and K.F. Jensen, "Analysis of Thermal Management in a Microfabricated High-Temperature Fuel Processor," *Chem. Eng. Sci.* (submitted)

9. L.R. Arana, N. de Mas, R. Schmidt, A.J. Franz, M.A Schmidt and K.F. Jensen, "Isotropic Etching of Silicon in Fluorine Gas for MEMS Micromachining," *Journal Microelectromechanical Systems* (submitted)

7.2 <u>Patents</u>

1. L. R. Arana, A. J. Franz, K. F. Jensen, S. B. Schaevitz, M. A. Schmidt, "Thermally Efficient Micromachined Device," US Patent Application filed Aug 2001

7.3 <u>Presentations</u>

7.3.1. <u>Invited</u>

1. L.R. Arana, C.D. Baertsch, R.C. Schmidt, M.A. Schmidt, K.F. Jensen, "Microchemical Reactors for Thermally Efficient Fuel Processing," Materials Research Society, Fall Meeting, Boston, MA (Nov. 2002).

2. K.F. Jensen, "Towards integrated microsystems for chemical synthesis" Plenary in Micro Total Analysis Systems (μ-TAS) 2002, Nara, Japan

3. K.F. Jensen, "Chemical and Biological Microsystems," Frontiers of Technology, Industrial Research Institute, San Ramon, CA, March 2004

4. K.F. Jensen, "Thermal Management and Integration Challenges for Microreactor based Power Sources", Thermal Management for Micro and Meso Power systems, Chicago, Il 2004

7.3.2. Contributed

1. S. B. Schaevitz, A. J. Franz, K. F. Jensen, and M. A. Schmidt, "A Combustion-Based MEMS Thermoelectric Power Generator," Transducers '01 Munich, Germany, June 2001.

2. L. R. Arana, A. J. Franz, S. B. Schaevitz, K. F. Jensen, and M. A. Schmidt, Microchemical Systems for Fuel Processing: Hydrogen Production in a Microfabricated Reactor/Heat Exchanger, presented at the Annual Meeting of the American Institute of Chemical Engineers, Nov., 2001

3. L. R. Arana, S. B. Schaevitz, A. J. Franz, K. F. Jensen, and M. A. Schmidt, "A Microfabricated Suspended-Tube Chemical Reactor for Fuel Processing," oral presentation at MEMS 2002, Las Vegas, NV USA, January 2002.L. R. Arana, S. B. Schaevitz, A. J. Franz, K. F. Jensen, and M. A. Schmidt, "A Suspended-Tube Microreactor for Thermally-Efficient Fuel Processing," at IMRET 6, New Orleans, LA USA, March 2002

4. L.R. Arana, K.F. Jensen, and M.A. Schmidt, "Catalytic Hydrogen Production in a Microfabricated Chemical Reactor," to be presented at the Annual Meeting of the American Institute of Chemical Engineers, Nov., 2002

5. L.R. Arana, C.D. Baertsch, R.C. Schmidt, M.A. Schmidt, K.F. Jensen, "Combustion-Assisted Hydrogen Production in a High-Temperature Chemical Reactor/Heat Exchanger for Portable Fuel Cell Applications," 12th International Conference on Solid-State Sensors, Actuators, and Microsystems (Transducers '03), Boston, MA, 2003.

6. Nielsen, L.R. Arana, C.D. Baertsch, M.A. Schmidt, K.F. Jensen, "A thermophotovoltaic Micro-Generator for Portable Power Applications," 12th International Conference on Solid-State Sensors, Actuators, and Microsystems (Transducers '03), Boston, MA, 2003.

7. B.A. Wilhite, M.A. Schmidt, and K.F. Jensen, "Palladium Based Micromembranes for Hydrogen Purification: Influence of Material Selection upon Performance," presented at the Annual Meeting of the American Institute of Chemical Engineers, San Francisco, CA, Nov 2003